JEM Journal of Experimental Medicine

ARTICLE

An iron-rich subset of macrophages promotes tumor growth through a Bach1-Ednrb axis

Ian W. Folkert[1,2,3,4*], William A. Molina Arocho[2,5*], Tsun Ki Jerrick To[2,5], Samir Devalaraja[2,5], Irene S. Molina[2,5], Jason Shoush[2,5], Hesham Mohei[2,5], Li Zhai[5], Md Naushad Akhtar[17], Veena Kochat[7], Emre Arslan[7], Alexander J. Lazar[7,8], Khalida Wani[9], William P. Israel[7], Zhan Zhang[10], Venkata S. Chaluvadi[5], Robert J. Norgard[6], Ying Liu[5], Ashley M. Fuller[5], Mai T. Dang[5,11,12], Robert E. Roses[3], Giorgos C. Karakousis[3], John T. Miura[3], Douglas L. Fraker[3], T.S. Karin Eisinger-Mathason[5], M. Celeste Simon[1,13], Kristy Weber[14], Kai Tan[15,16], Yi Fan[17], Kunal Rai[7], and Malay Haldar[1,2,5]

We define a subset of macrophages in the tumor microenvironment characterized by high intracellular iron and enrichment of heme and iron metabolism genes. These iron-rich tumor-associated macrophages (iTAMs) supported angiogenesis and immunosuppression in the tumor microenvironment and were conserved between mice and humans. iTAMs comprise two additional subsets based on gene expression profile and location—perivascular (pviTAM) and stromal (stiTAM). We identified the endothelin receptor type B (Ednrb) as a specific marker of iTAMs and found myeloid-specific deletion of *Ednrb* to reduce tumor growth and vascular density. Further studies identified the transcription factor *Bach1* as a repressor of the iTAM transcriptional program, including *Ednrb* expression. Heme is a known inhibitor of Bach1, and, correspondingly, heme exposure induced *Ednrb* and iTAM signature genes in macrophages. Thus, iTAMs are a distinct macrophage subset regulated by the transcription factor Bach1 and characterized by Ednrb-mediated immunosuppressive and angiogenic functions.

Introduction

The success and limitations of current immunotherapies have generated tremendous interest in how antigen-presenting cells (APCs) in the tumor microenvironment (TME) regulate antitumor immune responses. The two primary APC populations within the TME are tumor-associated macrophages (TAMs) and dendritic cells (DCs). Effective antitumor T cell responses depend upon APCs first taking up and processing antigens from tumor cells within the TME and migrating to draining lymph nodes, where they present antigen to prime cytotoxic T cells, which will in turn migrate to the tumor and kill tumor cells (Chen and Mellman, 2013). In most untreated cancer patients, this "cancer immunity cycle" is inhibited at multiple steps. However, the cellular and molecular basis of ineffective immune responses in the TME is not fully understood and represents the next frontier in cancer immunotherapy (Chen and Mellman, 2013; Motz and Coukos, 2013).

Macrophages are often the most abundant leukocyte present in the TME (Devalaraja et al., 2020; Gubin et al., 2018). Tissue macrophages display impressive functional diversity and can switch from a proinflammatory to an anti-inflammatory role depending on microenvironmental cues (Haldar and Murphy, 2014; Murray, 2017). This functional plasticity is often co-opted by tumors to grow, spread, and avoid immune responses (DeNardo and Ruffell, 2019). Importantly, tumor-associated macrophages (TAMs) often drive resistance to current modalities of cancer immunotherapy, including immune checkpoint blockade (DeNardo and Ruffell, 2019; Arlauckas et al., 2017). While T-cell-based immunotherapies have dramatically altered

[1]Abramson Family Cancer Research Institute, Perelman School of Medicine, University of Pennsylvania, Philadelphia, PA, USA; [2]Institute for Immunology, Perelman School of Medicine, University of Pennsylvania, Philadelphia, PA, USA; [3]Department of Surgery, Perelman School of Medicine, University of Pennsylvania, Philadelphia, PA, USA; [4]Department of Surgical Oncology, The University of Texas MD Anderson Cancer Center, Houston, TX, USA; [5]Department of Pathology and Laboratory Medicine, Perelman School of Medicine, University of Pennsylvania, Philadelphia, PA, USA; [6]Department of Medicine, Perelman School of Medicine, University of Pennsylvania, Philadelphia, PA, USA; [7]Department of Genomic Medicine and MDACC Epigenomics Therapy Initiative, MD Anderson Cancer Center, Houston, TX, USA; [8]Department of Anatomical Pathology, The University of Texas MD Anderson Cancer Center, Houston, TX, USA; [9]Department of Translational Molecular Pathology, The University of Texas MD Anderson Cancer Center, Houston, TX, USA; [10]Department of Bioengineering, University of Pennsylvania, Philadelphia, PA, USA; [11]Division of Neurology, Children's Hospital of Philadelphia, Philadelphia, PA, USA; [12]Department of Neurology, Washington University in St. Louis Schoold of Medicine, St. Louis, MO, USA; [13]Department of Cell and Developmental Biology, Perelman School of Medicine, University of Pennsylvania, Philadelphia, PA, USA; [14]Department of Orthopedic Surgery, Perelman School of Medicine, University of Pennsylvania, Philadelphia, PA, USA; [15]Division of Oncology and Center for Childhood Cancer Research, Children's Hospital of Philadelphia, Philadelphia, PA, USA; [16]Department of Pediatrics, Perelman School of Medicine, University of Pennsylvania, Philadelphia, PA, USA; [17]Department of Radiation Oncology, Perelman School of Medicine, University of Pennsylvania, Philadelphia, PA, USA.

*I.W. Folkert and W.A. Molina Arocho contributed equally to this paper. Correspondence to Malay Haldar: mhaldar@pennmedicine.upenn.edu.

the treatment paradigm for many solid tumors, a significant proportion of patients fail to respond or develop resistance (Benci et al., 2016; Kalbasi and Ribas, 2020; Pitt et al., 2016). Hence, identifying and targeting pathways that regulate macrophage states within the TME is key to overcoming current limitations of cancer immunotherapy. Furthermore, targeting macrophages may simultaneously impact other aspects of tumor biology, including invasion and angiogenesis (Noy and Pollard, 2014; Zhou et al., 2020), making these cells an especially appealing target.

Here, we identify a distinct subset of iron-rich TAMs (iTAMs) within the murine and human TME. iTAMs are characterized by the downregulation of antigen presentation and antitumor immune response pathways and the upregulation of pathways involved in heme metabolism and angiogenesis. Using co-transplantation experiments, we show that iTAMs promote both angiogenesis and tumor growth. Further transcriptomic analysis using single-cell and bulk RNA sequencing (RNA-seq) identified the endothelin receptor type B (*Ednrb*) as a specific marker of iTAMs. Myeloid-specific deletion of *Ednrb* leads to decreased vascular density and tumor growth. We also identify the transcriptional repressor Bach1 as a regulator of the iTAM gene expression program and show that fibrosarcoma (FS) tumors transplanted into Bach1 KO mice are characterized by increased tumor growth. Finally, we show that pharmacological inhibition of endothelin signaling can enhance responses to immune checkpoint inhibitors.

Results

The TME contains a distinct subset of iron-rich macrophages (iTAMs)

TAMs are a heterogeneous population, and the subset-specific functions of TAMs remain poorly understood (Qian and Pollard, 2010; DeNardo and Ruffell, 2019; Zhou et al., 2020; Noy and Pollard, 2014). To identify potentially important but rare TAM subsets, we performed single-cell RNA-seq (scRNA-seq) of FAC-sorted CD45$^+$ leukocytes from syngeneic FS flank tumors in C57BL/6 mice (Fig. 1 A). Using a combination of canonical marker genes and reference-based annotation with SingleR (Fig. S1, A and B), we confirmed that TAMs are the most abundant leukocytes in the FS microenvironment (Fig. 1 B). Further examination of the macrophage clusters revealed two closely related TAM clusters (clusters 6 and 12, murine FS scRNA-seq dataset) that expressed high levels of heme oxygenase 1 (*Hmox1*)—a key enzyme in heme degradation (Fig. 1 C). Relative to all other leukocytes, these two TAM clusters also highly expressed genes involved in heme and iron metabolism such as the heme transporter *Hrg1* (*Slc48a1*), ferritins (*Fth1* and *Ftl1*), and the hemoglobin-haptoglobin scavenging receptor *Cd163* (Fig. 1 D). Correspondingly, gene set enrichment analysis (GSEA) showed enrichment in heme metabolism pathways in these two TAM clusters relative to all other leukocyte clusters (Fig. 1 E). These TAMs also selectively expressed high levels of marker genes with no known direct association with heme or iron metabolism such as *Ednrb*, *Cd36*, *Lyve1*, and *Mmp12* (Fig. 1 D). Therefore, these transcriptionally defined clusters likely mark distinct TAM subsets.

To explore the existence of these TAM subsets in other murine tumors, we performed scRNA-seq of tumor-infiltrating leukocytes on two distinct genetically engineered mouse models of sarcoma—synovial sarcoma (SS) and undifferentiated pleomorphic sarcoma (UPS) (Haldar et al., 2007; Kirsch et al., 2007). Unlike transplantation-based models, these Cre-LoxP-based conditional mouse models recapitulate the natural course of tumors—from induction to progression. TAMs were abundant in both tumor types (Fig. 1, F and H; and Fig. S1, C and E). Importantly, both tumors harbored TAM clusters with increased expression of iron metabolism genes, albeit at different frequencies compared with FS tumors (Fig. 1, G and I). These cells also selectively expressed the same non-heme/iron-related genes that marked these clusters in FS tumors (Fig. 1, G and I). Similar to the FS tumors, the GSEA of these macrophage clusters in SS and UPS tumors showed significant enrichment for heme metabolism (Fig. S1, D and F).

We reasoned that increased expression of heme and iron metabolism genes in these TAMs likely indicated high levels of intracellular iron, which would endow them with ferromagnetic properties. Thus, we developed a two-step magnetic column-based protocol to enrich these cells from tumors and verify their high iron content. Briefly, single-cell suspensions from FS tumors were passed over magnetic columns. Both the flow-through (iron-negative cellular fraction) and the eluate (iron-positive cellular fraction) were collected and further subjected to macrophage enrichment through F4/80 selection beads on a second set of magnetic columns (Fig. 2 A). The second enrichment with F4/80 beads ensures that only macrophages (TAMs) are isolated from the iron-negative fraction. For the iron-positive fraction, the second enrichment step ensures (1) identical processing of both iron-high TAMs and other TAMs and (2) removal of cells that were weakly adherent to the magnetic column in the first enrichment step due to lower intracellular iron and/or non-specific binding. As a control for this enrichment process, we used the spleen, where red pulp macrophages (RPMs) act as the primary storage site for heme-derived iron (Alam et al., 2017). Similar to the spleen, iron-fractionated macrophages from tumors were characterized by high intracellular iron (Fig. 2, B and C; and Fig. S2 A). Quantitative RT-PCR (RT-qPCR) showed significantly higher expression of the two key heme and iron-metabolism–associated genes—*Hmox1* (enzyme degrading heme) and *Slc40a1* (iron exporter)—in the iron-positive macrophages, suggesting enrichment of the two previously identified TAM clusters in the iron-positive fraction from tumors (Fig. S2 B). Thus, we refer to these two TAM clusters as iron-rich TAMs or iTAMs henceforth.

To validate this more rigorously, we performed scRNA-seq on the iron-positive and iron-negative TAMs from the magnetic column-based approach described above. Using a combination of canonical marker genes and reference-based annotation with SingleR (Fig. S2, C–E), we first confirmed that the vast majority of both the iron-positive and iron-negative fractions are indeed macrophages (Fig. 2 D). Key iTAM marker genes such as *Hmox1*, *Slc40a1*, *CD163*, and *Ftl1* were used to identify the iTAM clusters

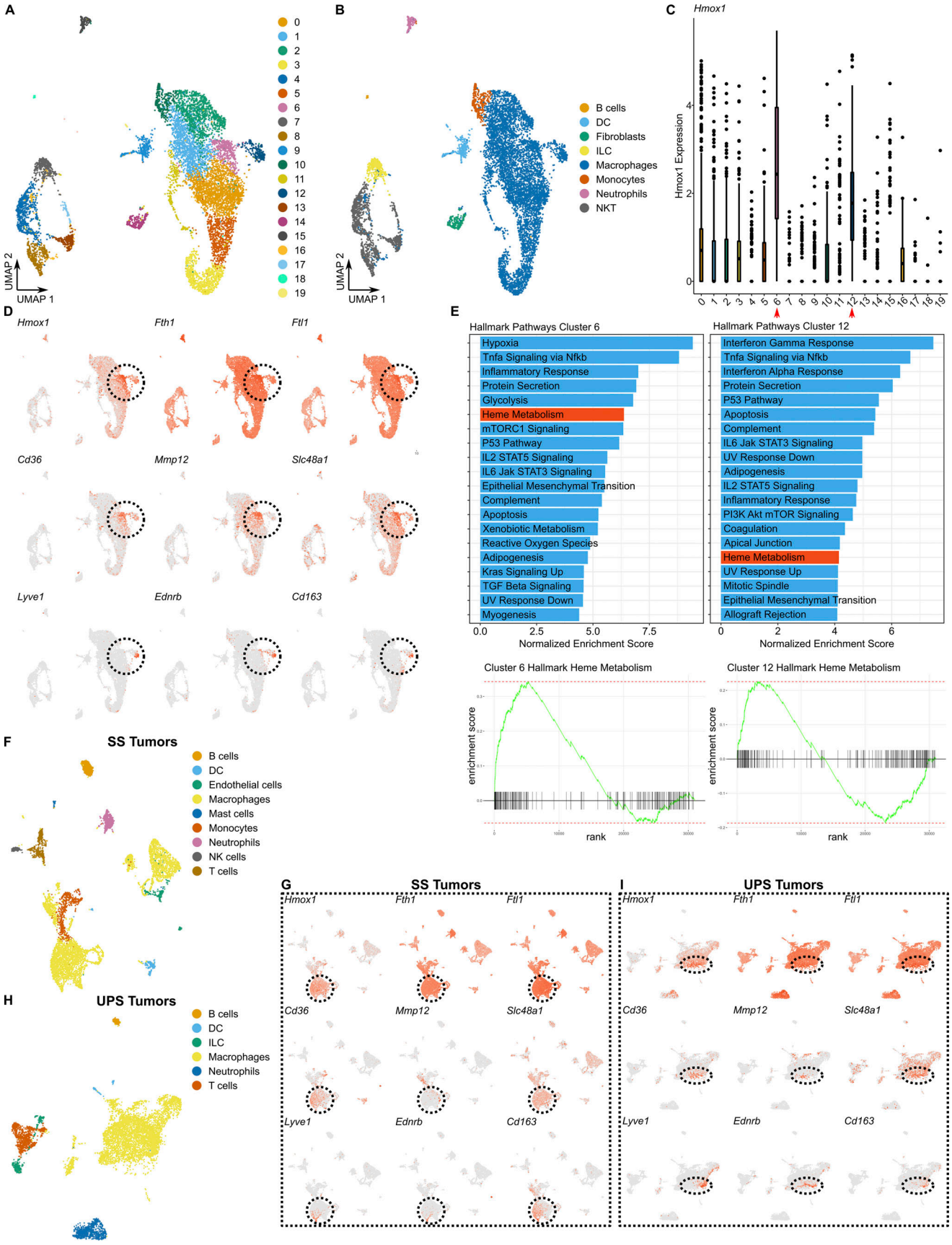

Figure 1. **scRNA-seq identifies TAM subsets enriched for heme metabolism. (A)** UMAP of CD45⁺ immune cells sorted from murine FS tumors and profiled using scRNA-seq (murine FS scRNA-seq dataset, *n* = 2 mice). Cells from the two replicates were combined prior to sequencing, yielding one sequencing dataset.

Numbers represent distinct clusters. **(B)** UMAP of the murine FS scRNA-seq dataset showing cell-type annotation using the SingleR package with the ImmGen database as a reference for cell-type-specific gene expression signature. **(C)** Boxplot of *Hmox1* expression showing highest expression in two TAM clusters—6 and 12. **(D)** UMAP expression plots of selected top marker genes for clusters 6 and 12 in FS tumors. Clusters with the highest levels of expression of the indicated genes are encircled. Hmox1: Heme oxygenase 1. Fth1: Ferritin heavy polypeptide 1. Ftl1: Ferritin light polypeptide 1. Cd36. Mmp12: Matrix metallopeptidase 12. Slc48a1: Solute carrier family 48, member 1. Lyve1: Lymphatic vessel endothelial hyaluronan receptor 1. Ednrb: Endothelin receptor type B. Cd163: Cluster of differentiation 163. **(E)** GSEA of clusters 6 and 12 relative to all other clusters in the murine FS scRNA-seq dataset with normalized enrichment scores of the top 20 Hallmark gene sets from the Molecular Signatures Database (MSigDB). Pathways related to heme metabolism are highlighted in red. **(F)** UMAP of CD45$^+$ immune cells sorted from a murine model of SS and profiled using scRNA-seq (murine SS scRNA-seq dataset, n = 1 tumor). Cell types are annotated using the SingleR package with the ImmGen database as a reference for cell-type-specific gene expression signatures. **(G)** UMAP expression plots of selected top marker genes for clusters 6 and 12 in FS tumors within the murine SS scRNA-seq dataset. Clusters with the highest levels of expression are encircled. **(H)** UMAP of CD45$^+$ immune cells sorted from a murine model of UPS and profiled using scRNA-seq (murine UPS scRNA-seq dataset, n = 1 tumor). Cell types are annotated using the SingleR package with the ImmGen database as a reference for cell-type-specific gene expression signatures. **(I)** UMAP expression plots of selected top marker genes for clusters 6 and 12 in FS tumors within the murine UPS scRNA-seq dataset. Clusters with the highest levels of expression are encircled. NK: Natural Killer Cells. ILC: Innate Lymphoid Cells. DC: Dendritic Cells.

within this dataset (Fig. 2 D). Overall, both iron-positive and iron-negative fractions contained similar frequencies of leukocytes and macrophages (Fig. S2, F and G). Importantly, as anticipated, the iron-positive fraction contained a higher proportion of iTAMs compared with the iron-negative group (Fig. 2, E and F). This corresponded to a global increase in the expression of iTAM marker genes in the iron-positive fraction (Fig. 2 G). Finally, we validated iTAM enrichment through our magnetic column protocol with FCM using iTAM-associated cell surface markers identified in our scRNA-seq datasets and for which good commercial antibodies were available—CD163, Lyve1, and CD36 (Fig. 2, H–J). Of note, each step in our magnetic column-based iTAM enrichment protocol led to an incremental increase in the iTAM fraction, culminating in the highest proportion within the "final" iTAM fraction (Fig. S2 H).

Taken together, data presented in this section demonstrate the presence of a distinct subset of macrophages in murine tumors that are characterized by high intracellular iron and a distinct gene expression profile.

iTAMs express endothelin receptor type B (Ednrb) and are conserved between mice and humans

In our analyses of scRNA-seq of murine TAMs, the Endothelin receptor type b (Ednrb) stood out as a specific marker of iTAMs with unknown functions in TAMs (Fig. 1, D, G, and I). Correspondingly, the iron-positive fraction of magnetically enriched TAMs (as described above) showed significantly higher *Ednrb* (up to 40×) and this corresponded with increased binding of a fluorescent endothelin 1 (ligand for Ednrb) peptide by FCM (Fig. 3, A and B). Thus, we use Ednrb as a marker for iTAMs henceforth and further explore its functions and regulation within iTAMs in the later sections of this manuscript.

We next asked whether iTAMs are also present in human tumors by examining publicly available scRNA-seq datasets. Since we primarily used murine sarcoma models to characterize iTAMs, we examined a scRNA-seq dataset of 12 human SS (Jerby-Arnon et al., 2021). Tumor cells, immune infiltrates, and other stromal components were identified in this dataset (Fig. 3 C). Major immune cell types were identified based on the expression of hallmark genes, including macrophages (Fig. 3 D). Importantly, we identified a subset of macrophages displaying a gene expression signature consistent with iTAMs, including *EDNRB* (Fig. 3, E and F). Human and murine iTAM clusters were enriched for similar gene sets, including heme metabolism (Fig. 3 G). ScRNA-seq of another unrelated human tumor, melanoma, also revealed the presence of iTAMs (Jerby-Arnon et al., 2018) (Fig. 3, H–J). Looking across a variety of tumor types in The Cancer Genome Atlas (TCGA), we found a positive correlation between *EDNRB* expression and other iTAM marker genes, further supporting our hypothesis that iTAMs are present in a variety of human tumors and that Ednrb is a conserved marker for both human and murine iTAMs (Fig. S3 A).

In summary, human tumors harbor iTAMs that recapitulate the transcriptional characteristics and Ednrb expression of their murine counterparts.

iTAMs originate from monocytes and comprise two spatially distinct subsets

The two iTAM clusters identified in our FS model shared expression of genes involved in heme and iron metabolism but were also characterized by unique markers and transcriptional profiles (Fig. 4, A and B). One of these two iTAM clusters (cluster 3, iron fractionated TAM scRNA-seq dataset) highly expressed many of the previously published markers (Chakarov et al., 2019) of perivascular macrophages (Fig. 4 C). Thus, we termed the two iTAM clusters perivascular iTAMs (pviTAMS) and stromal iTAMs (stiTAMs). GSEA comparing each iTAM cluster to all other TAM clusters in the dataset revealed that the two iTAM clusters are enriched for many of the same gene sets including heme metabolism, hypoxia, and TNF signaling pathways. stiTAMs are uniquely enriched for glycolysis while pviTAMs are enriched for other inflammatory response pathways (Fig. 4, D and E). We next asked whether iron content within pviTAMs and stiTAMs correlates with expression levels of the genes that characterize these two iTAM clusters. As noted in Fig. 2 F, iTAM clusters are found in both iron-positive and iron-negative fractions after magnetic enrichment, albeit at lower frequency within the iron-negative fraction. Importantly, we found that many of the stiTAM and pviTAM marker genes (Fig. 4, F and G) were expressed at higher levels in the iron-enriched fraction of stiTAMs and pviTAMs, respectively, when compared to their iron-negative counterparts. Thus, iron levels within cells in these clusters correlate with expression levels of several marker genes that define these clusters.

Given the gene expression differences between pviTAMs and stiTAMs, we wondered whether these two TAM subsets might

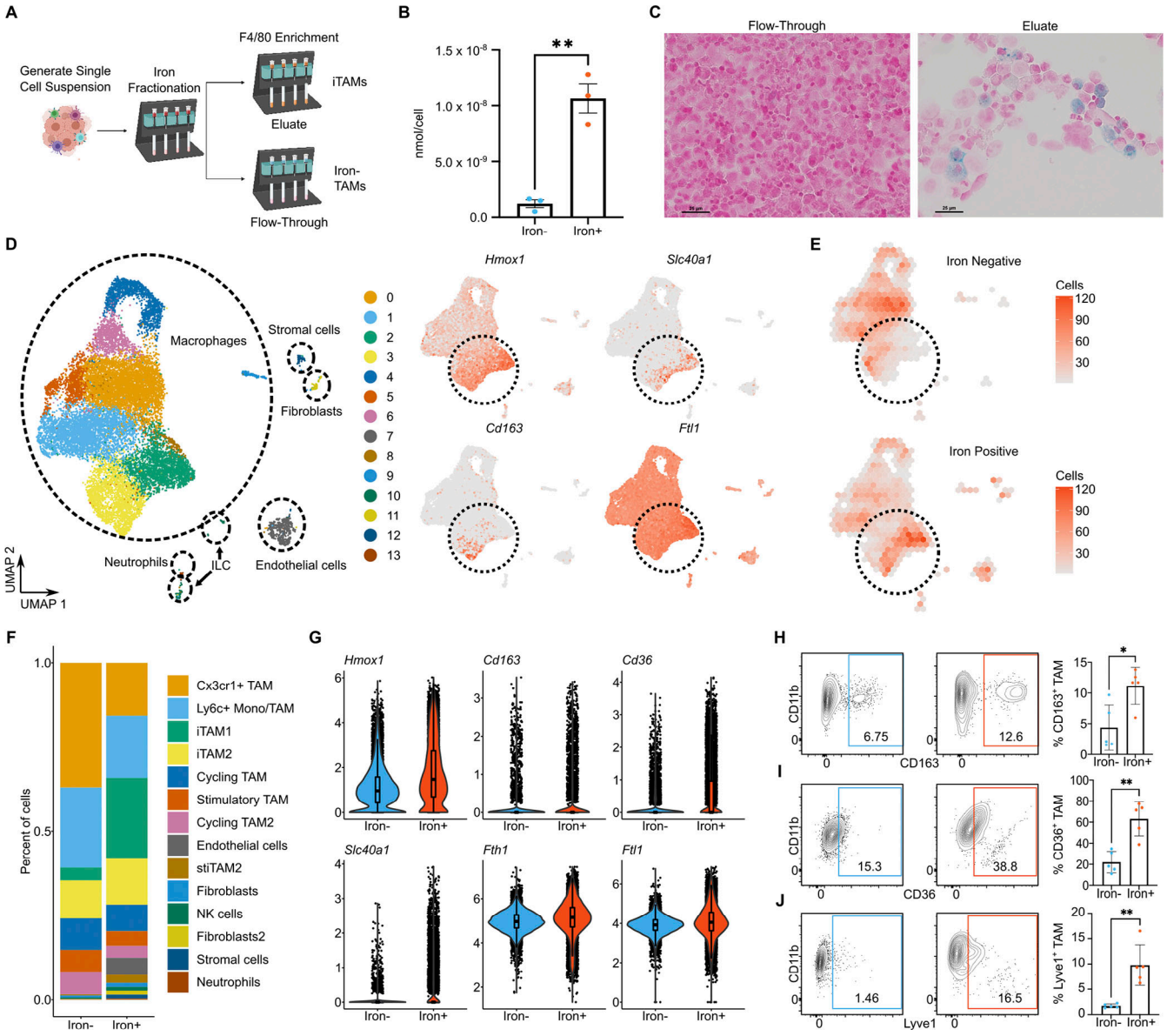

Figure 2. **iTAMs are characterized by high intracellular iron. (A)** Schematic for iron fractionation and iTAM enrichment. Tumors are digested into singlecell suspensions and directly passed over a magnetic column (Miltenyi). Iron-negative cells pass through the column, while iron-positive cells are bound and subsequently eluted. To further enrich for TAMs, both the iron-positive and iron-negative fractions are incubated with anti-F4/80 magnetic beads and passed over a second fresh column. **(B)** Iron quantification (Abcam) of iron-negative and iron-positive TAMs after enrichment from FS tumors as described in A (n = 3 mice per group). Approximately 4.4 × 10^6 cells were used to measure iron in the flow-through and eluate fractions. Representative of three independent experiments. **(C)** Prussian blue staining for intracellular iron performed on cytospin preparations of iron fractionated TAMs (as described in A) from murine FS tumors. **(D)** The left panel shows UMAP with annotated cell types of iron-negative (flow-through, n = 2 mice) and iron-positive (eluate, n = 2 mice) TAMs isolated using the workflow depicted in A and profiled using scRNA-seq (iron fractionated TAM scRNA-seq dataset). Replicates within each group were combined prior to sequencing, yielding one iron-negative and one iron-positive sample. Cell types are annotated using the SingleR package with the ImmGen database as a reference for cell-type-specific gene expression signature. The right panel shows UMAP expression plots of genes involved in heme and iron metabolism (*Hmox1*, *Slc40a1*, *Cd163*, *Ftl1*) in the iron fractionated TAM scRNA-seq dataset. Macrophage clusters with the highest levels of expression of these genes are encircled. **(E)** Density plots of iron-negative and iron-positive samples from the iron fractionated TAM scRNA-seq dataset. Macrophage clusters corresponding to iTAMs are encircled and show increased numbers of iTAMs in the iron-positive fraction. **(F)** Bar plot showing the percent contribution from each cluster in the iron-negative and iron-positive samples from the iron fractionated TAM scRNA-seq dataset. iTAM1 and iTAM2 correspond to the two distinct clusters of iTAMs seen in the murine FS scRNA-seq dataset. **(G)** Expression of genes involved in heme and iron metabolism (*Hmox1*, *Cd163*, *Cd36*, *Slc40a1*, *Fth1*, and *Ftl1*) in the iron-negative and iron-positive samples in the iron fractionated TAM scRNA-seq dataset. **(H)** FCM plots (left) and frequencies (right) of CD163$^+$ TAMs (CD45$^+$CD11b$^+$F4/80^{high}) in iron-negative (left FCS plot) and iron-positive (right FCS plot) TAMs fractionated from FS tumors. Pregated on live singlets, CD45$^+$, Ly6G$^-$, CD11b$^+$, and F4/80^{high} (n = 5 mice). Representative of ≥3 independent experiments. **(I)** FCM plots (left) and frequencies (right) of CD36$^+$ TAMs (CD45$^+$CD11b$^+$F4/80^{high}) in iron-negative (left FCS plot) and iron-positive (right FCS plot) TAMs fractionated from FS tumors. Pregated on live singlets, CD45$^+$, Ly6G$^-$, CD11b$^+$, and F4/80^{high} (n = 5 mice). Representative of ≥3 independent experiments. **(J)** FCM plots (left) and frequencies (right) of Lyve1$^+$ TAMs (CD45$^+$CD11b$^+$F4/80^{high}) in iron-negative (left FCS plot) and iron-positive (right FCS plot) TAMs fractionated from FS tumors. Pregated on live singlets, CD45$^+$, Ly6G$^-$, CD11b$^+$, and F4/80^{high} (n = 5 mice). Representative of ≥3 independent experiments. *P < 0.05, **P < 0.01. Statistical significance was determined by using the Mann–Whitney U test. Bar graphs are plotted as mean with SEM. All FCM plot events were pregated on live singlets unless otherwise specified and numbers represent the percentage of cells within the highlighted gates.

Figure 3. **Ednrb expression marks iTAMs in mice and humans. (A)** Relative expression (RT-qPCR) of *Ednrb* in paired iron fractionated TAMs (as described in Fig. 2 A) from flank FS tumors (n = 4 mice per group). Representative of ≥3 independent experiments. **(B)** FCM plots of iron-negative (flow-through) and iron-

positive (eluate) cells from FS tumors (as described in Fig. 2 A but without the second step of F4/80+ cell enrichment) stained with ET1-HF488 conjugated peptide (fluorescent ligand for Ednrb). Histogram shows cells pregated on live singlets, CD45$^+$ cells. Representative of three independent experiments. **(C)** t-SNE plot of malignant, immune, and stromal cells from 12 human SS profiled using scRNA-seq (human SS dataset) by Jerby-Arnon et al. (2021). Cluster labels from the original publication are highlighted. Pre-processed data from the original publication was downloaded from the Broad Institute Single Cell Portal (https://singlecell.broadinstitute.org/single_cell). **(D)** t-SNE expression plots of marker genes specific to major leukocyte and stromal cell types in the human SS scRNA-seq dataset, with clusters corresponding to TAMs encircled. **(E)** t-SNE expression plots of select iron metabolism and iTAM marker genes in the human SS scRNA-seq dataset, with myeloid clusters with the highest expression (clusters C1.immune and C13.immune) encircled. **(F)** Heatmap showing expression of selected iTAM marker genes identified in the murine FS scRNA-seq dataset, shown by cluster in the human SS scRNA-seq dataset. Clusters C1.immune and C13.immune demonstrate the highest expression of these iTAM markers. **(G)** GSEA of cluster C13.immune relative to all other clusters in the human SS scRNA-seq dataset, with normalized enrichment scores of the top 25 Hallmark pathways from the MSigDB shown and the Heme metabolism gene set highlighted in red. **(H)** t-SNE plot of leukocytes and stromal cells from 31 human melanoma tumors profiled using a publicly available scRNA-seq dataset (human melanoma scRNA-seq dataset) from a published study (Jerby-Arnon et al., 2018). Pre-processed data from the original publication was downloaded from the Broad Institute Single Cell Portal (https://singlecell.broadinstitute.org/single_cell). **(I)** t-SNE expression plots of marker genes specific to major leukocyte and stromal cell types in the human melanoma scRNA-seq dataset, with clusters corresponding to TAMs encircled. **(J)** t-SNE expression plots of select iron metabolism and iTAM marker genes in the human melanoma scRNA-seq dataset, with myeloid clusters with the highest expression encircled. ***P < 0.001. Statistical significance was determined by using the Mann-Whitney U test. Bar graph is plotted as mean with SEM. All FCM plot events were pregated on live singlets unless otherwise specified and numbers represent the percentage of cells within the highlighted gates.

have distinct origins. Tissue and tumor macrophages can originate from circulating monocytes (monocyte-derived macrophages) or embryonic precursors (Haldar and Murphy, 2014). To address this, we obtained the Ms4a3^{Cre} mice that express Cre recombinase in monocytes and their progeny (Liu et al., 2019). These mice were bred to the Rosa^{tdTomato} reporter mice, and the resulting Ms4a3^{Cre}: Rosa^{tdTomato} mice were transplanted subcutaneously with syngeneic FS tumor cells. Analyses of tdTomato-expressing TAMs from these tumors revealed predominantly monocyte origin for both pviTAMs and stiTAMs (Fig. 4 H). We selected CD163 and CD36 as pviTAM and stiTAM markers, respectively, based on their differential expression between the two iTAM subsets (as shown in Fig. 4, A and B) and the availability of reliable commercial antibodies.

We next explored whether stiTAMs and pviTAMs were indeed differentially localized in the TME—a difficult endeavor with traditional imaging methods given the overlapping gene expression pattern between the two clusters. We began with our recently published computational approach (CytoTalk) to determine cell–cell interaction from scRNA-seq data (Hu et al., 2021). Remarkably, iTAMs were determined to preferentially interact with endothelial cells (Fig. 5 A). We believe that this computationally predicted association comes from the pviTAM component of the overall iTAM gene expression signature used in CytoTalk. Consistent with this, immunofluorescence of murine UPS tumors showed a predominantly perivascular distribution of Ednrb$^+$ pviTAMs, while Hmox1$^+$ stiTAMs were more uniformly distributed throughout the tumor stroma (Fig. 5, B and C). A major limitation of immunofluorescence is the limited number of markers that can be simultaneously queried. Thus, we next performed spatial transcriptomic analyses (Xenium, 10X Genomics) on human melanomas (Fig. 5 D; and Fig. S3, B and C; and Tables S1 and S2). Here, we confirmed that macrophages with gene expression hallmarks of pviTAMs were predominantly located next to blood vessels. Remarkably, we also found large numbers of stiTAMs localizing close to hemorrhagic areas within the tumor (Fig. 5 D; and Fig. S3, B and C). Thus, stiTAMs likely represent erythrophagocytic macrophages in the TME. Of note, *EDNRB* expression was prominent in pviTAMs and sparsely expressed in stiTAMs (Fig. 5 D). This is consistent with our scRNA-seq data where *Ednrb* expression was significantly higher in the pviTAM cluster, although the difference was not as stark as in our human Xenium data.

In summary, we describe two subsets of iTAMs that differ in their gene expression profile and location but are both derived from monocytes.

iTAMs support tumor growth through angiogenesis and immunosuppression

We next explored the function of iTAMs in the TME. As shown above, heme and iron metabolism are not the only overrepresented pathways in iTAMs, which also includes immune response and inflammatory pathways (Fig. 4, D and E). Despite its advantages for identifying unique cell types and sub-populations, scRNA-seq has lower sensitivity compared to bulk RNA-seq, especially for low-abundance transcripts (Svensson et al., 2017; Chen et al., 2019). Therefore, to deeply probe for differentially expressed genes in iTAMs, we performed bulk RNA-seq to compare iron-positive and iron-negative TAMs enriched over magnetic columns as described above. We found 278 significantly downregulated and 1,361 significantly upregulated genes in iTAMs compared to iron-negative TAMs (adjusted P value <0.1 and logFC >0.5), with Ednrb as one of the most upregulated genes (Fig. 6 A). As anticipated, the samples clustered based on their iron fractionation status, rather than tumor of origin (Fig. 6 B). Gene Ontology (GO) terms related to blood vessels and endothelial cells as well as extracellular matrix organization were enriched in upregulated genes in the iron-positive TAMs (Fig. 6 C). On the other hand, GO terms related to inflammatory response, cytokine signaling, and T cell activity were enriched in iron-negative TAMs (Fig. 6 D). Thus, both scRNA-seq and bulk RNA-seq analyses suggest a pro-angiogenic and anti-inflammatory function of iTAMs. These sequencing data were further corroborated by lower levels of proinflammatory TAM markers in the iron-positive fraction by FCM (Fig. 6, E and F).

To directly examine the impact of iTAMs on tumor growth, iron-positive and iron-negative TAMs were isolated using magnetic columns as described above, mixed with FS cells (1:1), and the tumor-TAM mix transplanted subcutaneously into

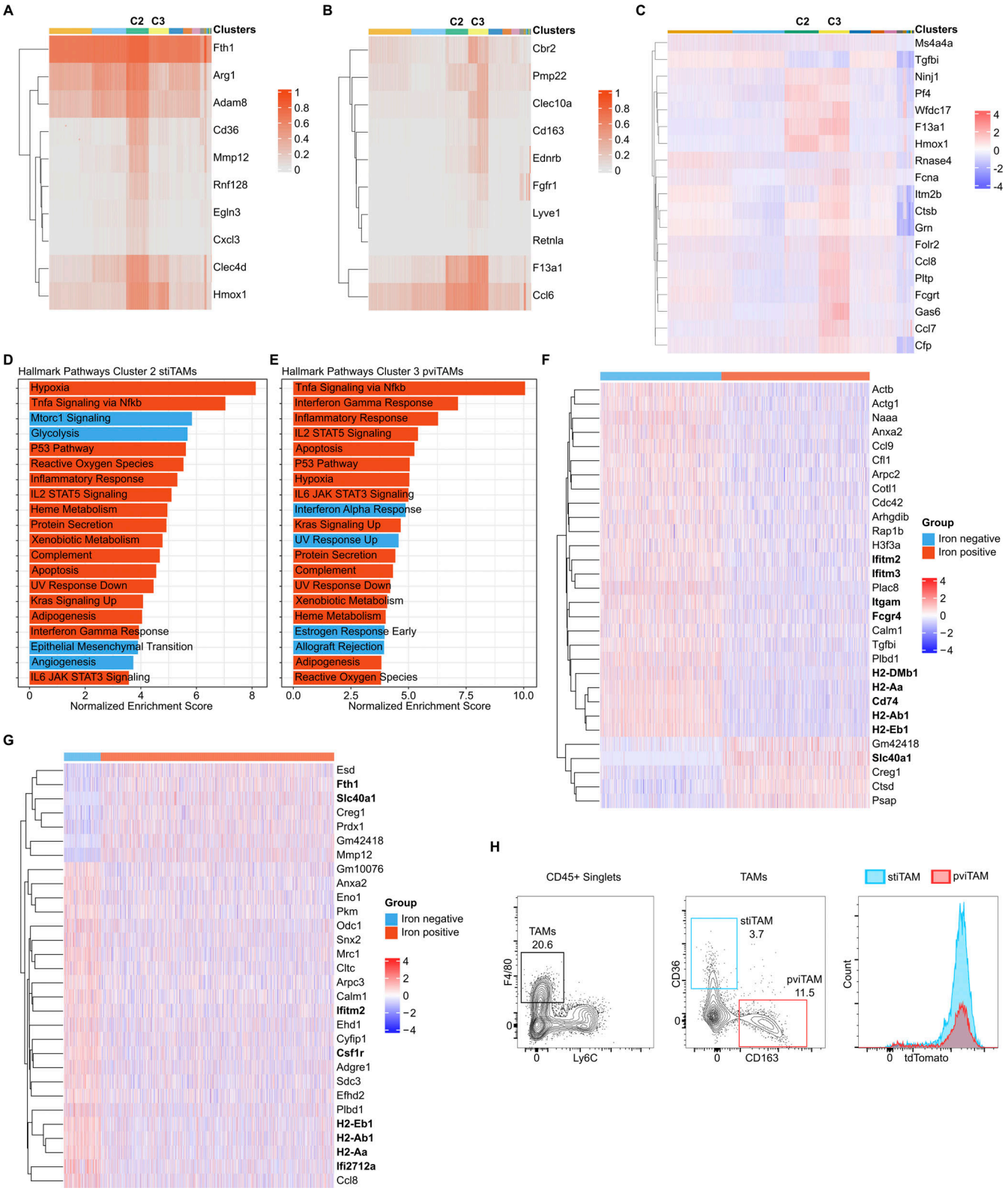

Figure 4. **iTAMs comprise two distinct subsets. (A and B)** Heatmap showing that the two iTAM clusters (green and yellow color-coded) of the iron fractionated scRNA-seq dataset demonstrate high expression of the top 10 iTAM marker genes identified in the murine FS scRNA-seq dataset (clusters 6 and 12 in Fig. 1). The green color-coded cluster is also referred to as cluster 2 (C2) and the yellow as cluster 3 (C3) elsewhere in this figure. **(C)** Heatmap showing expression of perivascular macrophage marker genes by cluster within the iron fractionated TAM scRNA-seq dataset. The genes defining perivascular macrophages were identified from a previously published scRNA-seq dataset of perivascular macrophages (Chakarov et al., 2019). C3 (the yellow color-coded TAM cluster) has the highest relative expression of the perivascular marker genes compared to all other clusters, including C2 (the green color-coded) cluster. **(D and E)** GSEA of stiTAMs (C2, green color-coded cluster in A–C) and pviTAMs (C3, yellow color-coded cluster in A–C) relative to all other clusters, with

normalized enrichment scores of the top 20 Hallmark gene sets from the MSigDB shown. Pathways enriched in both clusters are highlighted in red, while pathways uniquely enriched in one cluster are highlighted in blue. **(F)** Heatmap of the top 30 differentially expressed genes between the iron-negative and iron-positive cells within the stiTAM cluster of the iron fractionated TAM scRNA-seq dataset. Genes involved in iron metabolism, antigen presentation, or the generation of immune or inflammatory responses are bolded. **(G)** Heatmap of the top 30 differentially expressed genes between the iron-negative and iron-positive cells within the pviTAM cluster of the iron fractionated TAM scRNA-seq dataset. Genes involved in iron metabolism, antigen presentation, or the generation of immune or inflammatory responses are bolded. **(H)** Representative FCM of single-cell suspension from murine FS generated in Ms4A3^{Cre}:Rosa26^{tdTomato} mice. The gating scheme is indicated for each histogram and the numbers represent the percentage of cells enclosed within the box. The two-color histogram on the right shows the distribution of cells expressing the monocyte lineage marker TdTomato within pviTAMs (red) and stiTAMs (blue).

syngeneic C57BL/6J mice. iTAM-containing tumors grew significantly faster and harbored more endothelial cells and fewer T cells overall (Fig. 6, G–J). Tumor growth differences between experimental groups persisted up to 2 wk after transplantation, but the magnitude of difference reduced over time, which is likely due to the limited lifespan of the cotransplanted macrophages (Devalaraja and Haldar, 2020). We confirmed the existence, albeit at reduced levels, of the cotransplanted macrophages as well as the retention of their macrophage phenotype in our cotransplantation model by genetically labeling the transplanted macrophages (Fig. S4 A).

Despite lower overall T cell infiltration, we did not observe consistent differences in T cell activation in tumors co-transplanted with iTAMs compared with control (Fig. S4 B). Again, this is likely due to the fact that (1) cotransplanted iTAMs are lost over time due to their limited lifespan and (2) both TAM and iTAM cotransplanted tumors generate their own iTAMs de novo over time. Thus, the difference in iTAM frequency between the experimental groups disappears over time. As T cells also have a finite lifespan and continuously infiltrate tumors, any iTAM-mediated difference in their activation status between experimental groups will also disappear over time. To directly examine the impact of iTAMs on T cells, we isolated iTAMs from tumors using FCM-based cell sorting. From our scRNA-seq data, we identified Folate receptor beta (Folr2) as one of the surface markers enriched in iTAMs and used it to isolate these cells (Fig. 7, A and B). While both iTAMs and other TAMs suppressed the proliferation of activated T cells in vitro, iTAMs were significantly more potent, especially to CD4 T cells (Fig. 7, C–F).

We next directly examined the impact of iTAMs on angiogenesis in an in vitro tube formation assay. We first enriched iTAMs using our magnetic column protocol and cultured the cells in M-CSF for several days to enrich for macrophages and remove other contaminating cell types. iTAMs and iron-negative TAMs obtained in this way were cocultured with endothelial cells to examine their impact on tube formation—a common assay for angiogenesis. iTAMs were significantly better than other TAMs in supporting various aspects of angiogenesis such as overall tube length, number of segments, and overall mesh area (Fig. 7 G). In parallel, we also devised an alternative approach to generate iTAM-like macrophages in vitro. Macrophages were generated by culturing bone marrow cells in M-CSF (Bone Marrow Derived Macrophages or BMDMs). These cells were then exposed to heme to generate iTAM-like macrophages (Fig. S4 C). Notably, these in vitro–generated iTAM-like cells also promoted angiogenesis in a tube formation assay (Fig. 7 H).

Thus, iTAMs support tumor growth, angiogenesis, and suppress T cell activity within the TME.

Ednrb supports the protumor function of iTAMs

As shown above, *Ednrb* expression marks iTAMs (Fig. 1, D, G, and I). *Ednrb* encodes a G protein-coupled receptor that binds three endothelin ligands (Endothelin 1, 2, and 3) to activate a variety of context-dependent second messenger systems (Dagamajalu et al., 2021). Endothelins are produced by endothelial cells while *Ednrb* is predominantly expressed in pviTAMs, indicating the existence of an Edn–Ednrb communication axis between pviTAMs and blood vessels. Indeed, our CytoTalk analyses (Fig. 5 A) identified Edn1–Ednrb interactions between iTAMs and endothelial cells. To explore this further, we first deleted *Ednrb* in TAMs by obtaining a floxed Ednrb (Ednrb$^{flox/flox}$) mouse (Rattner et al., 2013) and breeding it to the Lysozyme 2-Cre (LysM^{Cre}) mouse. As the Ednrb$^{flox/flox}$ mice were only available to us in a mixed genetic background, we depleted T cells in LysM^{Cre}:Ednrb$^{flox/flox}$ and control (littermates with intact *Ednrb* expression) mice prior to subcutaneously transplanting them with FS cells (C57BL/6 background). *Ednrb* was deleted efficiently in macrophages by this approach (Fig. S4, D–F). Importantly, loss of *Ednrb* in macrophages led to reduced tumor growth and increased surface MHC-II expression on TAMs (Fig. 8, A–C). Loss of Ednrb signaling in TAMs also reduced vascular density based on the frequency of CD31$^+$ endothelial cells (Fig. 8 D).

These findings suggest that Edn signaling in TAMs affects tumor growth through the regulation of both angiogenesis as well as anti-tumor immune responses. As mentioned above, a limitation of the conditional genetic deletion of *Ednrb* in TAMs is the requirement for T cell depletion prior to tumor transplantation as the tumor cells and the Ednrb$^{flox/flox}$ mice have different genetic backgrounds and are immunologically incompatible. A potent small molecule inhibitor of Edn signaling—Macitentan—is commercially available and, although it is a dual endothelin receptor antagonist, it can be used to examine the overall impact of endothelin signaling on tumor growth in immunocompetent mice. Monotherapy with macitentan showed a trend toward smaller tumors, albeit not statistically significant. Thus, we next combined macitentan with PD1 inhibition, finding significantly smaller tumors and a trend toward improved survival with the combination therapy (Fig. 8, E and F). Macitentan treatment did not lead to weight loss in vivo or affect FS tumor cell viability in vitro, except at very high concentrations (Fig. S4, G and H). Based on this observation, we next asked whether *EDNRB* expression levels might predict responses to immune checkpoint therapy. In one publicly available dataset for human

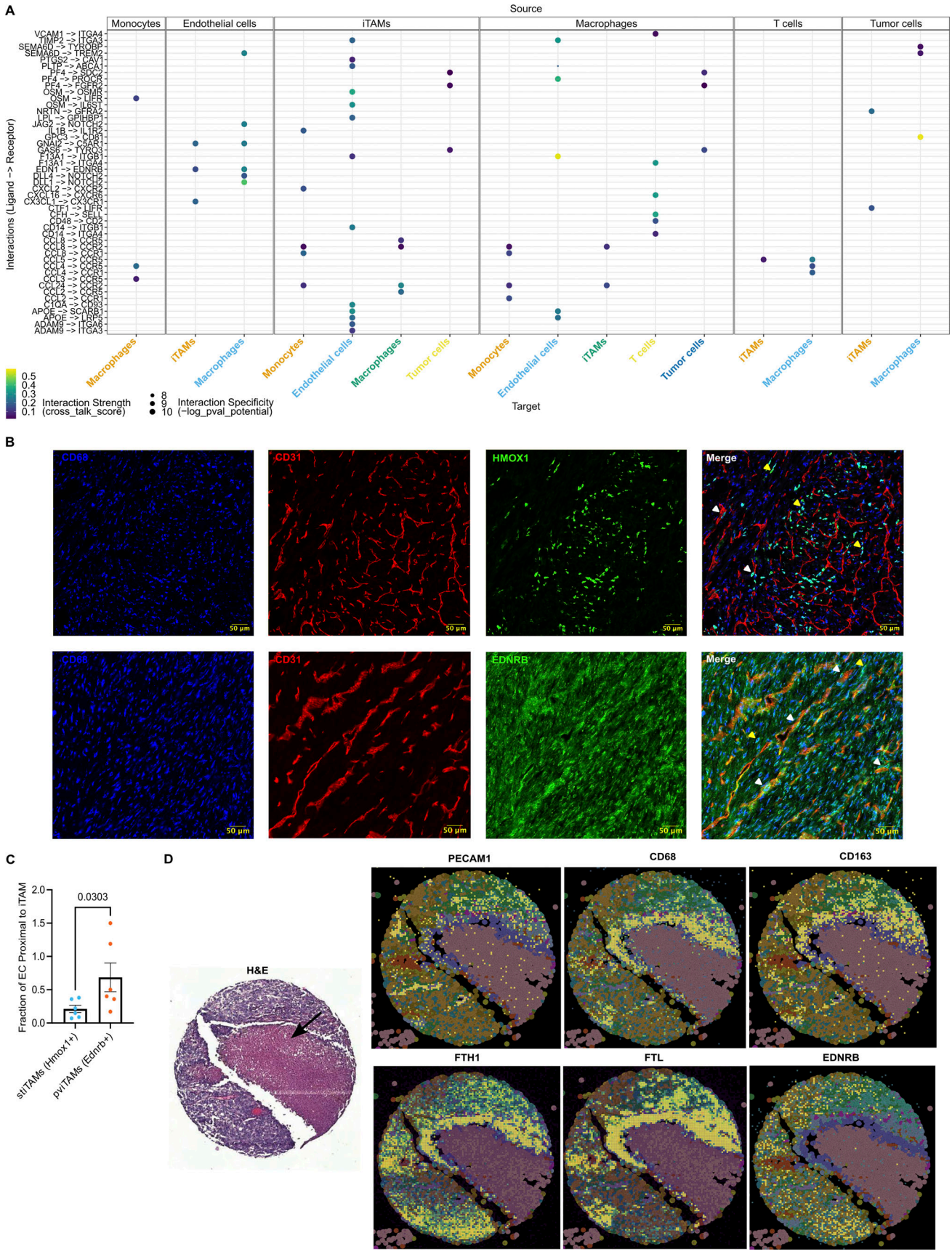

Figure 5. **pviTAMs and stiTAMs have distinct localization in tumors. (A)** Cell–cell signaling network generated from the murine SS scRNA-seq dataset (Fig. 1 F) using the CytoTalk computational algorithm. The y-axis lists the ligand–receptor interactions. Cells participating in the interactions are listed above

(cellular source of ligand) and below (cells with receptor) the graph. The size and color of dots indicate the specificity and strength of the interaction, respectively. **(B)** Immunofluorescence images of murine UPS showing the location of pviTAMs (white arrowhead) and stiTAMs (yellow arrowhead). Tumor sections were stained with anti-CD31 (red; endothelial cells), anti-CD68 (blue; macrophages), and anti-Hmox1 (top; green) or anti-Ednrb (bottom; green). Scale bar: 50 µm. Representative of two experiments. **(C)** Relative quantification of the fraction of endothelial cells ($CD31^+$) proximal to iTAM population ($Hmox1^+$ stiTAM or $Ednrb^+$ pviTAM). The number of endothelial cells and $Hmox1^+$ or $Ednrb^+$ cells was determined in each region of interest. Each symbol represents a region of interest where counting was performed within one representative stained tumor section. **(D)** Spatial transcriptomics (Xenium—10X Genomics) was performed on a human melanoma tissue microarray. The panel of genes tested included multiple iTAM marker genes. The leftmost panel shows H&E staining for the selected section in a tissue microarray of human melanoma biopsies. The black arrow highlights a large hemorrhagic area within the tumor. The six fluorescence panels show the expression of selected iTAM genes (headers) that were included in the Xenium panel. Statistical significance was determined by using the Mann-Whitney U test. Bar graph is plotted as mean with SEM.

melanoma patients, we found that *EDNRB* expression was significantly lower in tumors of patients who responded to nivolumab monotherapy (Riaz et al., 2017) (Fig. 8 G). Notably, Ednrb expression was a better predictor of response in this dataset compared to established markers such as PD1, PD-L1, or CTLA4 (Fig. 8 G).

Finally, we asked whether the presence and extent of iTAMs might correlate with an immunosuppressive microenvironment in human tumors. We found that many of the iTAM marker genes, including *EDNRB*, were associated with increased T cell dysfunction scores across many of the datasets queried (Fig. 8 H). Thorsson and colleagues previously conducted a thorough immunogenomic analysis of >10,000 tumors from TCGA, representing 33 diagnostic subtypes to characterize six distinct TME subtypes—wound healing, IFN-γ dominant, inflammatory, lymphocyte depleted, immunologically quiet, and TGF-β dominant (Thorsson et al., 2018). Notably, *EDNRB* was one of the most significant differentially expressed immunomodulators within the immunologically quiet subgroup (C5), which was characterized by high levels of immunosuppressive M2 macrophages and monocytes, and the lowest numbers of tumor-infiltrating lymphocytes (Fig. 8 I).

Taken together, the findings described in this section demonstrate the pleiotropic tumor-promoting effects of Edn-Ednrb signaling in iTAMs.

Bach1 regulates the iTAM transcriptional program

To explore the molecular regulation of iTAM development and function, we performed transcription factor binding motif enrichment analyses for both subsets of iTAMs using GSEA. Both iTAM subsets were enriched for motifs corresponding to transcription factors in the Bach and Nrf2 families (Fig. 9, A and B). *Bach1* and *Bach2* immediately stood out as heme-regulated transcription factors (Igarashi and Watanabe-Matsui, 2014). Bach1 heterodimerizes with small Maf (Maf-F, G, and K) transcription factors to repress target genes. Intracellular heme can bind Bach1 to induce its degradation through the proteasome, allowing small MAFs to bind the Nrf2 transcription factor, which induces target gene transcription (Sun et al., 2004). Importantly, we previously demonstrated that heme-induced degradation of Bach1 plays a critical role in the development of iron-recycling macrophages in the spleen (Haldar et al., 2014). Thus, we next investigated whether heme-induced Bach1 degradation may also regulate iTAM development and function. We began by performing scRNA-seq on $CD45^+$ leukocytes isolated from FS tumors generated in Bach1 WT and Bach1 KO mice (Fig. 9 C; and Fig. S4, I and J). Of note, Bach1 KO mice are on a mixed background, requiring T cell depletion prior to tumor cell transplantation to avoid immune rejection. Consistent with our hypothesis that Bach1 is a transcriptional repressor of the iTAM program, Bach1 KO tumors harbored a greater proportion of iTAMs and a lower proportion of stimulatory TAMs (Fig. 9 D and Fig. S5 A). Globally, the immune infiltrates of Bach1 KO tumors were characterized by dramatic downregulation of genes involved in antigen presentation (*Cd74*, *H2-Aa*, *B2m*) and upregulation of genes involved in heme and iron metabolism (*Hmox1* and *Slc40a1*) (Fig. 9 E). Looking just within the iTAMs, we observed a similar pattern, with significant downregulation of genes involved in antigen presentation (*Cd74*, *H2-Aa*, *H2-Ab1*, and *H2-Eb1*) and significant upregulation of genes involved in heme metabolism (*Hmox1*, *Slc40a1*, *Slc48a1*, *Ftl1*, *Fth1*, *Spic*) as well as additional iTAM marker genes (*Pf4*, *F13a1*, and *Mmp12*) in Bach1 KO iTAMs (Fig. 9 F). GSEA comparing iTAMs of the two genotypes identified over-representation of many iTAM-associated gene sets (heme metabolism and angiogenesis) and lower enrichment of gene sets associated with antitumor immune responses (allograft rejection, IFN response) in Bach1 KO (Fig. 9 G and Fig. S5 B).

Consistent with these transcriptional changes, we found lower surface expression of MHCII in iTAMs from Bach1 KO mice, supporting the notion that Bach1 loss (genetic deletion or heme-induced protein degradation) induces an immunosuppressive TAM phenotype (Fig. 9, H and I). Importantly, these transcriptional and phenotypic changes within TAMs translated into significant increases in both tumor volume and tumor weight in Bach1 KO mice (Fig. 9, J and K). Tumors generated in Bach1 KO mice also showed a trend toward higher vascular density based on the frequency of $CD31^+$ cells (Fig. S5 C). As mentioned above, heme is known to act as an inhibitor of the transcriptional repressor Bach1 by inducing its degradation in a proteasome-dependent manner (Haldar et al., 2014). Correspondingly, heme exposure recapitulated the key transcriptional effects of Bach1 deficiency in monocyte-derived macrophages in vitro, including upregulation of Ednrb (Fig. S5, D–L). Taken together, these findings identify Bach1 as a master regulator of the iTAM transcriptional program, with genetic or heme-induced Bach1 degradation driving the development and expression pattern of iTAMs.

Intratumoral hemorrhage induces iTAM development

iTAMs are defined by selective upregulation of heme metabolism pathways and high intracellular iron content. We show

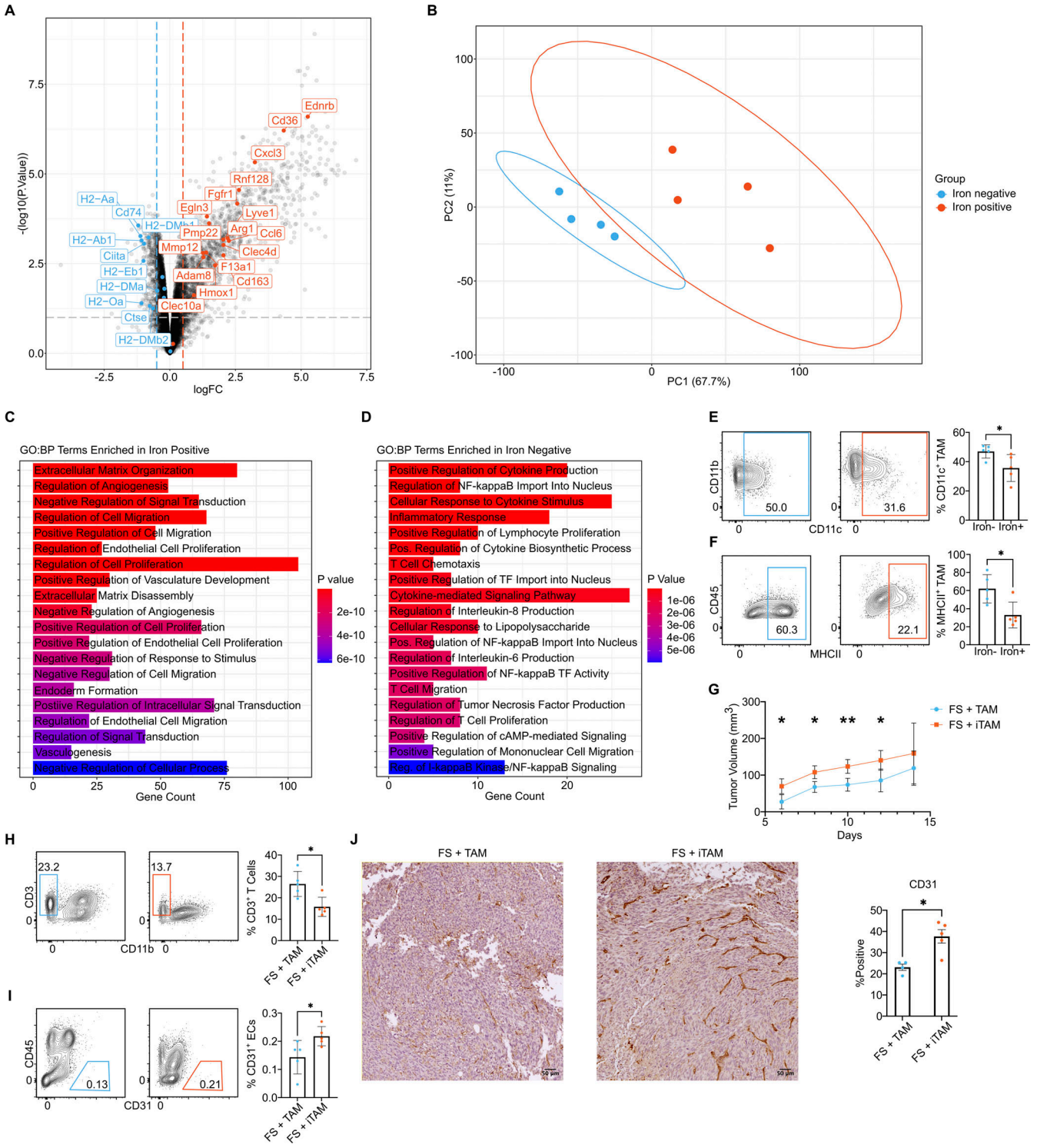

Figure 6. **iTAMs promote tumor growth. (A)** Volcano plot of differentially expressed genes (n = 278 downregulated and 1,361 upregulated genes with adjusted P value <0.1 and logFC >0.5) in bulk RNA-seq data from four pairs of iron-negative and iron-positive TAMs (bulk iron fractionated TAM RNA-seq dataset, see Fig. 3 A). Select significantly downregulated genes involved in antigen presentation through major histocompatibility complex class II (MHCII) are highlighted and labeled in blue (gene list from https://www.informatics.jax.org/go/term/GO:0019886 [GO Term: antigen processing and presentation of exogenous peptide antigen via MHC class II]). Significantly upregulated genes from the top 10 stiTAM markers and top 10 pviTAM markers from the murine FS scRNA-seq dataset are highlighted and labeled in red. **(B)** Principal component analysis (PCA) plot showing the first two principal components from the bulk iron fractionated TAM RNA-seq dataset. **(C)** Top 20 GO biological process (GO:BP) terms significantly enriched in upregulated genes in the iron-positive TAMs (bulk iron fractionated TAM RNA-seq dataset) based on the Enrichr R package. Pos. = positive, TF = transcription factor, Reg. = regulation. **(D)** Top 20 GO:BP terms significantly enriched in upregulated genes in the iron-negative TAMs (bulk iron fractionated TAM RNA-seq dataset) based on the Enrichr R package. Pos. = positive, TF = transcription factor, Reg. = regulation. **(E)** FCM plots (left) and frequencies (right) of CD11c$^+$ TAMs (CD45$^+$CD11b$^+$F4/80^{high}) in iron-negative

(left FCS plot) and iron-positive (right FCS plot) TAMs fractionated from FS tumors. Cells in the histogram were pregated on live singlets, CD45$^+$, Ly6G$^-$, CD11b$^+$, and F4/80^{high}. Representative of ≥3 independent experiments. **(F)** FCM plots (left) and frequencies (right) of MHCII$^+$ TAMs (CD45$^+$CD11b$^+$F4/80^{high}) in iron-negative (left FCS plot) and iron-positive (right FCS plot) TAMs fractionated from FS tumors. Cells in the histogram were pregated on live singlets, CD45$^+$, Ly6G$^-$, CD11b$^+$, and F4/80^{high}. Gates were drawn manually on individual samples to appropriately distinguish MHCII$^-$ and MHCII$^+$ populations in each sample. Representative of ≥3 independent experiments. **(G)** TAMs or iTAMs were isolated from murine FS using our magnetic column-based approach, mixed 1:1 with FS cells grown in culture, and the mixture was then injected subcutaneously into C57BL/6 mice. Tumors were measured every 2 days starting 6 days after implantation. Shown are tumor volumes over time (n = 4 tumors per group). Representative of four independent experiments. **(H)** FCM plots (left) and frequencies (right) of CD45$^+$CD3$^+$ T cells in iron-negative and iron-positive TAM co-transplanted tumors described above in Fig. 6 G. Cells in the histogram were pregated on live singlets, CD45$^+$ Ly6G$^-$. Representative of ≥3 independent experiments. **(I)** FCM plots (left) and frequencies (right) of CD45$^-$CD31$^+$ endothelial cells (ECs) in iron-negative and iron-positive TAM co-transplantated tumors described above in Fig. 6 G. Representative of ≥3 independent experiments. **(J)** Immunohistochemistry with anti-CD31 on tumors generated with iron-negative and iron-positive TAM cotransplanted tumors described above. Representative micrographs are on the left and quantification on the right. Scale bar: 50 µm. Representative of ≥2 independent experiments. *P < 0.05, **P < 0.01. Statistical significance was determined using the Mann-Whitney U test. The significance of differences in tumor volume (G) was determined using repeated-measures ANOVA. Bar graphs are plotted as mean with SEM. All FCM plot events were pregated on live singlets unless otherwise specified and numbers represent percentage of cells within the highlighted gates.

above the role of Bach1 in suppressing the iTAM transcriptional program and how heme-mediated degradation of Bach1 might induce iTAM development. We observed that the frequency of iTAMs varied significantly between the tumor types we tested, with the greatest abundance in SS tumors (Fig. S5 M). Interestingly, we often noticed spontaneous gross hemorrhage in our SS tumor model (Fig. S5 N). As described above in our human melanoma Xenium spatial analyses, stiTAMs often congregate near hemorrhagic areas. Taken together, these observations prompted us to hypothesize that intratumoral hemorrhage induces the development of iTAMs—especially stiTAMs. Additionally, hemorrhagic SS tumors harbored fewer inflammatory TAMs compared with non-hemorrhagic tumors by FCM (Fig. S5 O).

To dig deeper into the role of hemorrhage, we developed a mouse model for intratumoral hemorrhage (Fig. 10 A). In developing this model, we wished to extricate the effects of erythrocytes from other immune cells that also extravasate during hemorrhage. Hence, autologous anticoagulated blood from tumor-bearing mice (syngeneic subcutaneous FS) was centrifuged and the erythrocytes were suspended in buffered saline before injecting directly into the tumors of the same mice (Fig. 10 A). 2 days after erythrocyte (or vehicle) injection, single-cell suspensions from the tumors were subjected to orthogonal analyses including FCM and scRNA-seq (Fig. 10 A). Flow cytometry showed hemorrhagic tumors to harbor fewer immunostimulatory APCs (Fig. 10 B). These findings were consistent with FCM experiments we performed comparing spontaneously hemorrhagic SS tumors to non-hemorrhagic SS tumors above, where the hemorrhagic tumors harbored fewer CD11C$^+$ MHCII$^+$ APCs (Fig. S5 O). These observations were further supported by scRNA-seq (Fig. 10 C), which showed an increase in the proportion of iTAMs within the hemorrhagic tumors in our model system (Fig. 10 D). Differential expression analyses of pviTAMs from hemorrhagic and non-hemorrhagic tumors revealed significant upregulation of genes involved in iron metabolism (*Ftl1*, *Fth1*) and downregulation of genes involved in antitumor immune responses (*CD74*, *H2-Aa*, *H2-Eb1*, *H2-Ab1*) within the hemorrhagic tumors (Fig. 10 E).

Finally, we asked whether the links between hemorrhage and iTAMs are specific to the TME. In a recent manuscript, Askenase and colleagues performed longitudinal scRNA-seq of myeloid cells from peripheral blood and intracerebral hematomas of patients who suffered intracranial hemorrhage (Askenase et al., 2021). Their published dataset provided a unique opportunity to examine the expression of iTAM-associated genes in a hemorrhagic context outside of solid tumors. Remarkably, we found *EDNRB* and *HMOX1* were among the most highly induced genes in macrophages and monocytes within hematomas after intracerebral hemorrhage (Fig. 10 F).

In summary, the findings described in this manuscript identify iTAMs as a distinct TAM subset induced by heme-regulated Bach1 degradation and reveal a molecular communication between the tumor microvasculature and iTAMs through the endothelin signaling pathway (Fig. 10 G). These insights will pave the way for further research exploring iTAM biology and therapeutic approaches to target these cells.

Discussion

TAMs are abundant in many tumors and can either restrict or enhance antitumor immune responses through a variety of mechanisms (DeNardo and Ruffell, 2019). TAMs also contribute to immunotherapy resistance (Noy and Pollard, 2014), and treatment approaches that combine T cell activation with targeting of immunosuppressive myeloid cells may hold the key to overcoming treatment resistance. We describe here a unique subpopulation of heme-metabolizing, iron-rich TAMs within the TME. These iTAMs are characterized by the upregulation of pro-angiogenic pathways and downregulation of pathways involved in antigen presentation and immune stimulation. We also identified *Ednrb* as a potential therapeutic target specifically expressed by iTAMs and uncovered *Bach1* as a master regulator of the iTAM gene expression program. Our work elucidates an intriguing link between hemorrhage, heme metabolism, Bach1, immunosuppression, and angiogenesis within the TME.

iTAMs are defined by the presence of high levels of intracellular iron and the upregulation of heme metabolism pathways. Heme is an iron-centered porphyrin ring that is a key component of hemoglobin and responsible for oxygen delivery to tissues (Alam et al., 2017). Free heme is toxic and can lead to oxidative injury when released in tissues. Macrophages are the primary cell type responsible for heme scavenging and iron recycling, and they are capable of safely disposing of heme from

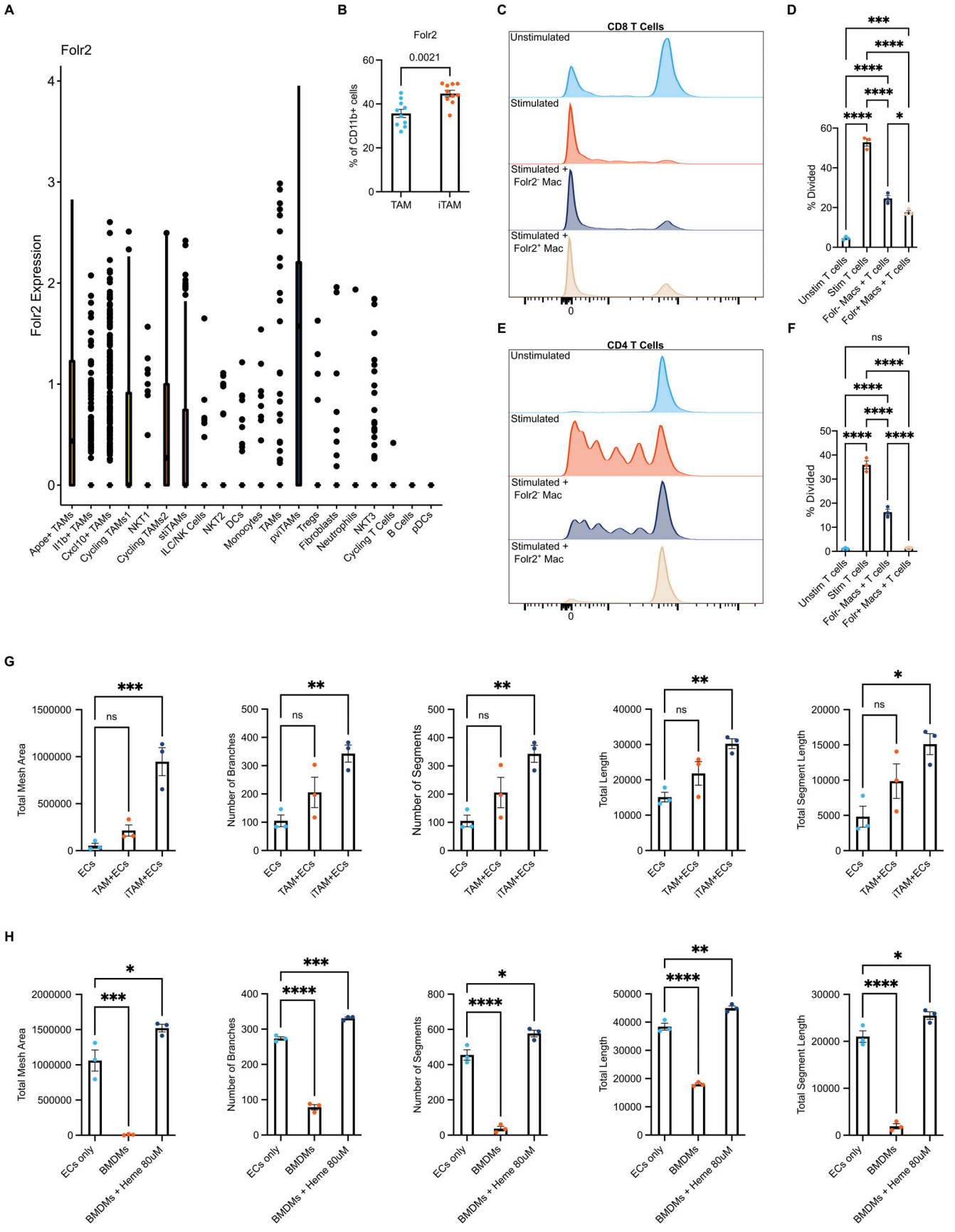

Figure 7. **iTAMs promote angiogenesis and immunosuppression. (A and B)** The left graph shows a boxplot of *Folr2* expression by cluster in the murine FS scRNA-seq dataset. The right bar graph inset shows cell surface expression of Folr2 measured by FCM in TAMs and iTAMs isolated from FS tumors using our

magnetic column-based enrichment outlined in Fig. 2 A (n = 5 mice; representative of three independent experiments). **(C and D)** Folr2 positive and negative TAMs were isolated using FCM-based cell sorting. These cells were then cocultured with T cells labeled with CTV dye. T cell proliferation was measured after 3 days based on dye dilution. T cell proliferation was significantly decreased after coculture with Folr2$^+$ macrophages. The colored histogram (C) shows representative dye dilution in CD8 T cells while the bar graph (D) quantifies CD8 T cell proliferation across multiple experimental replicates. Representative of ≥2 independent experiments. **(E and F)** The same experiment outlined above in panels C and D but showing CD4 T cell proliferation through a colored histogram (E) and bar graph quantification (F). **(G and H)** In vitro angiogenesis assay performed by coculturing macrophages with endothelial cells (x-axis). Various parameters of angiogenesis (y-Axis) were measured. Each symbol represents a different field of image in one cell culture well. Data is representative of three independent experiments. In (G) the macrophages used in the co-culture experiment were iron-negative TAMs or iTAMs derived from tumors. In (H) the macrophages were in vitro induced iTAMs generated by culturing bone marrow cells in M-CSF to generate macrophages (BMDMs) that were then exposed to heme (x-axis, BMDM + Heme) or control (x-axis, BMDMs). EC: Endothelial cells. ITAM: Iron-rich TAM. *P < 0.05, **P < 0.01, ***P < 0.001, ****P < 0.0001. Statistical significance in B was determined using the Mann-Whitney U test. Statistical significance in D and F–H was determined using repeated-measures ANOVA. Bar graphs are plotted as mean with SEM.

tissues (Alam et al., 2017). Macrophages can remove heme by phagocytosing old or damaged red blood cells (RBCs) and by taking up hemoglobin or heme via receptors such as CD163 and CD91, respectively (Soares and Hamza, 2016). We have previously shown that cell-extrinsic heme can act as a signaling molecule for macrophage differentiation in the spleen (Haldar et al., 2014). Besides differentiation, the effect of heme on macrophage function has been conflicting with both pro and anti-inflammatory effects described in the literature (Haldar et al., 2014; Pfefferlé et al., 2020; Vinchi et al., 2016). Many of these differences may be explained by variations in the model system, context, and the type of macrophage used. Our work here implicates heme as an immunomodulatory signaling molecule within the TME. In this context, it is important to note that macro- and microhemorrhage is common in solid tumors, which is often evident on imaging, histology, or at the time of surgical resection (Hashizume et al., 2000). Generally ascribed to "leaky" tumor vasculature, this phenomenon has been largely ignored outside of brain tumors, where bleeding is associated with adverse outcomes, and its impact on antitumor immunity is unclear. We find that at least a subset of iTAMs resemble perivascular macrophages. Based on their location, these perivascular TAMs are likely the first to encounter and phagocytose extravasated RBCs. Our data suggest that tumor microvascular dysfunction and RBC extravasation may regulate angiogenesis and immunosuppression through iTAMs.

Endothelin signaling has been previously implicated in several aspects of tumor progression (Nelson et al., 1995; Yin et al., 2003; Said et al., 2011). While a number of preclinical studies have focused on the role of the endothelin A receptor in promoting tumor growth in a tumor cell-intrinsic fashion (Yin et al., 2003; Said et al., 2011), the role of Ednrb in macrophage and tumor biology has not been adequately studied. Given that endothelins are primarily produced by endothelial cells in vivo, we were intrigued by the potential link between endothelin production, macrophage Ednrb activation, and angiogenesis. This link was even more interesting in light of the fact that at least a subset of iTAMs closely resemble perivascular macrophages that are known to play a role in regulating angiogenesis and vascular integrity (Chakarov et al., 2019; Lapenna et al., 2018). Despite the caveat of LysM-Cre being activated in neutrophils besides mononuclear phagocytes, we did not observe significant Ednrb expression in neutrophils, suggesting that neutrophils are unlikely to drive the observed tumor phenotypes in LsyM^{cre}:Ednrb$^{flox/flox}$ mice. Thus, our work suggests that perivascular iTAM Ednrb activation by locally produced endothelins may represent a novel pathway that promotes angiogenesis within the TME, and which can be targeted for therapeutic purposes. Besides Edn–Ednrb signaling, other surface receptors and pathways associated with iTAMs could also potentially be targeted—something we anticipate future work to clarify. Along these lines, it is interesting to note that CSF1-receptor (CSF1R) was expressed at lower levels in murine iTAMs (Fig. 4 G). Although human iTAMs did not show lower CSF1R expression, this is an important observation since CSF1R blockade is being tested in clinical trials to deplete immunosuppressive TAMs.

We elucidate here the role of the transcriptional repressor *Bach1* in both iTAM induction and *Ednrb* expression. This is particularly important in light of recent publications implicating BACH1 stabilization as an important factor in promoting tumor growth and metastasis in a tumor cell-intrinsic fashion (Lee et al., 2019; Lignitto et al., 2019). Lee et al. suggest that promoting Bach1 degradation with hemin could be an effective therapeutic strategy in triple-negative breast cancer (Lee et al., 2019), while Lignitto et al. demonstrate that Bach1 stabilization by Nrf2 is associated with increased transcription of pro-metastatic genes in lung adenocarcinoma (Lignitto et al., 2019). Our work elucidates an opposing role for *Bach1* in myeloid cells, with Bach1 loss in leukocytes promoting an immunosuppressive tumor immune infiltrate and increased tumor growth. One caveat of our approach is the use of a whole-body KO of Bach1. Nonetheless, there is very limited expression of this gene in hematopoiesis outside of the myeloid lineage and the tumor cells in our transplantation model were Bach1 sufficient. Thus, the effect of Bach1-KO on tumor growth very likely reflects the function of this gene within monocytes and macrophages, although confirmation would require the conditional deletion of this gene within mononuclear phagocytes. Thus, future attempts to target Bach1 must take a nuanced approach considering the disparate downstream effects of Bach1 in tumor and immune cells.

The identification, characterization, and functions of iTAMs described in this manuscript opens up several lines of important research in the future. One issue is whether and/or how high intracellular iron content of iTAMs might regulate their function and/or development. It is noteworthy that deleting Ednrb in macrophages did not alter intracellular iron levels in iTAMs nor did it affect the development of these cells. Furthermore, rapidly

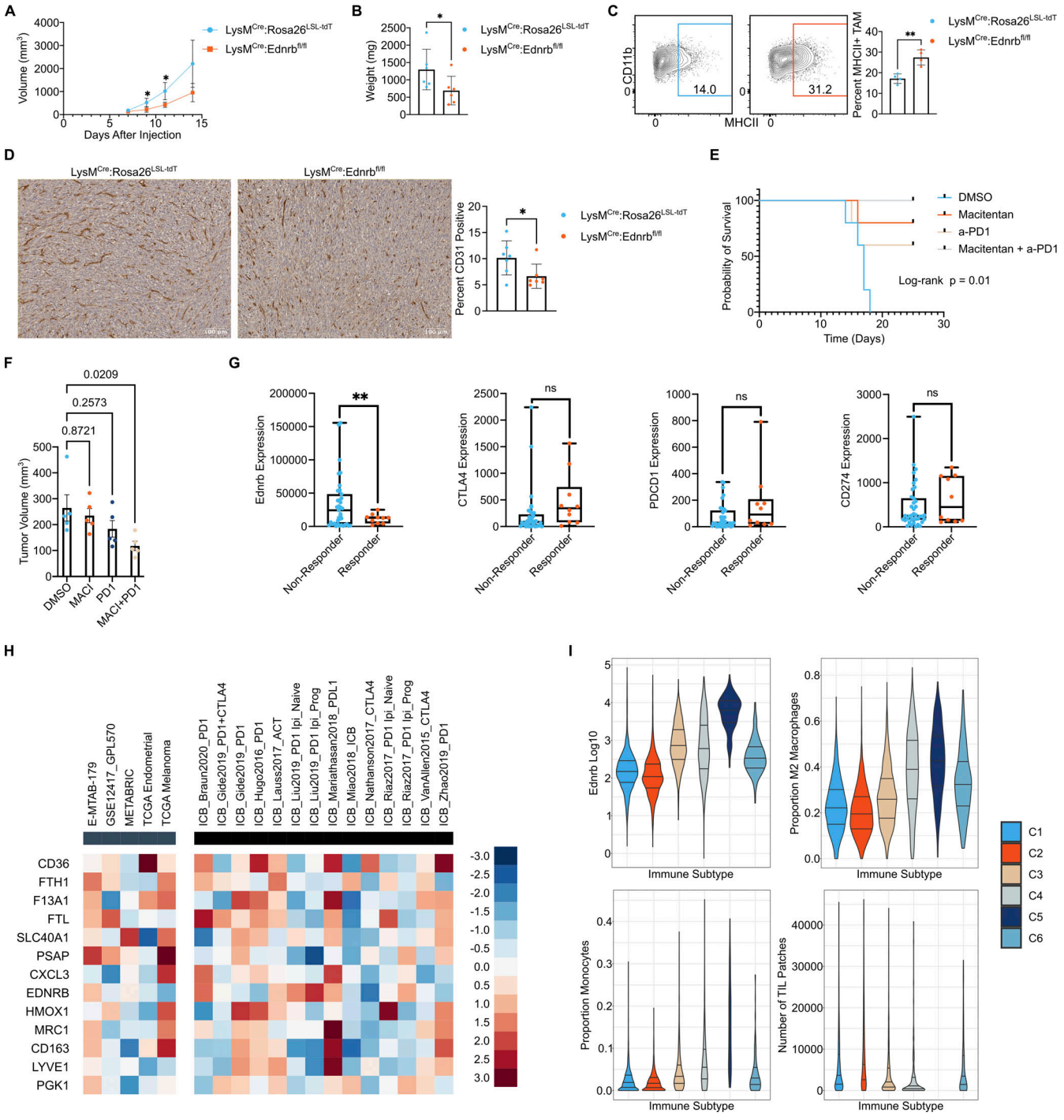

Figure 8. **Ednrb signaling promotes the tumor-supportive functions of iTAMs. (A)** Control mice (Lysm^{Cre}:Rosa$^{LSL\text{-}tdT}$) and mice with Ednrb deletion in macrophages (LysM^{Cre}:Ednrb$^{fl/fl}$) were transplanted subcutaneously with FS cells. Shown are tumor volumes over time (n = 6 mice per group). Representative of ≥3 independent experiments. **(B)** Weight of the tumors at endpoint from the experiment in A. **(C)** FCM plots (left) and frequencies (right) of MHCII$^+$ TAMs (CD45$^+$CD11b$^+$F4/80^{high}) in FS tumors generated in control (Lysm^{Cre}:Rosa$^{LSL\text{-}tdT}$) and Ednrb myeloid knockout (LysM^{Cre}:Ednrb$^{fl/fl}$) mice (n = 4 mice per group). Cells were pregated on live singlets, CD45$^+$, Ly6G$^-$, CD11b$^+$, and F4/80^{high}. Representative of ≥3 independent experiments. **(D)** Representative immunohistochemistry for CD31 in FS tumors generated in control (Lysm^{Cre}:Rosa^{tdT}) and Ednrb myeloid KO (LysM^{Cre}:Ednrb$^{fl/fl}$) mice. Scale bar: 100 µm. The bar graph on the right show quantification of % CD31 positive staining per tumor section (n = 7 tumors per group). Each dot represents a section/slide from an independent tumor. Representative of three independent experiments from two independent cohorts of tumors. **(E)** FS-bearing C57BL/6 mice were treated with the Endothelin receptor antagonist macitentan (i.p. 10 mg/kg, daily) or vehicle control (DMSO, daily) with or without anti-PD1 (200 µg, every 3 days) starting when tumors were ∼50 mm^3 (n = 5 tumors per group). Kaplan–Meier survival curves are shown, with a significant difference between groups by log-rank test (P = 0.01). Representative of two independent experiments. **(F)** Tumor volume measured at day 13 for the experiment outlined in E above (n = 5 tumors per group). **(G)** Expression of *EDNRB*, *CTLA4*, *PDCD1* (PD-1), and *CD274* (PD-L1) in human melanoma patients, stratified by response to treatment with nivolumab (Riaz et al., 2017). Raw data obtained from the CRI iAtlas portal (https://cri-iatlas.org/). **(H)** Z-scores of T cell dysfunction scores associated with each selected iTAM

marker gene in both the Core (grey) and Immunotherapy (black) datasets from the Tumor Immune Dysfunction and Exclusion (TIDE) database (http://tide.dfci.harvard.edu/). Higher Z-scores are associated with increased T cell dysfunction. **(I)** *EDNRB* expression in the tumor immune microenvironment subtypes identified by Thorsson et al. (2018), showing the highest expression in the "immunologically quiet" C5 subtype (leftmost panel), which is characterized by the highest proportion of M2 macrophages (top right panel) and monocytes (bottom left panel) and the fewest tumor-infiltrating lymphocytes (bottom right panel). Data downloaded from (https://cri-iatlas.org/). *P < 0.05, **P < 0.01. Significance for differences in tumor volume (A and F) were determined using repeated-measures ANOVA. Statistical significance in B–D was determined using the Mann-Whitney U test. Statistical significance in G was determined using a Student's *t* test. Bar graphs are plotted as mean with SEM. All FCM plot events were pregated on live singlets unless otherwise specified and numbers represent percentage of cells within the highlighted gates.

dividing tumor cells require iron, which might be provided by iTAMs through ferroportin. We anticipate future work to provide insights into these aspects of iTAM biology.

Materials and methods

Mice

Tumor models

Two distinct genetically engineered mouse models were used in this study: (1) mouse model of synovial sarcoma (Haldar et al., 2007) and (2) mouse model of undifferentiated pleomorphic sarcoma (Kirsch et al., 2007). Both models are Cre-inducible, where Cre is delivered via intramuscular injection of TAT-Cre fusion protein (Millipore Sigma). This approach mitigates the potential effects of viral vectors on the immune response. Syngeneic FS flank tumors were established in C57BL/6 mice purchased from Jackson Laboratories by transplantation of FS cells as described below.

Mononuclear phagocyte models

LysM^{Cre} mice were obtained from Jackson Laboratories and bred to: (1) Rosa26$^{LSL\text{-}tdT}$ and/or (2) Ednrb$^{flox/flox}$ mice. Bach1$^{-/-}$ mice were obtained from Jackson Laboratories and/or bred in-house for experimental use. The Rosa26$^{LSL\text{-}tdT}$ mice were purchased from Jackson Laboratories (Cat #007914) and harbors a LoxP-flanked stop cassette that prevents transcription of the tdT fluorescent reporter from a CAG promoter. Sex (including both male and female) and age-matched mice between 6 and 8 wk were used for these studies whenever possible. Mice were bred and maintained in specific pathogen–free facilities at the University of Pennsylvania. All animal procedures were conducted according to National Institutes of Health guidelines and approved by the Institutional Animal Care and Use Committee at the University of Pennsylvania.

Tumor cells

The C57BL/6 syngeneic FS cell line was previously described (Devalaraja et al., 2020). Tumor cell lines were cultured in DMEM with 10% FBS, 1% Pen/Strep, and 2 mM glutamine. Low-passage (<P15) cell lines were used for in vitro and in vivo experimentation. All cell lines were routinely tested and confirmed to be negative for mycoplasma contamination.

scRNA-seq analysis

Single-cell library preparation, sequencing, and pre-processing were performed by The Center for Applied Genomics (CAG) at the Children's Hospital of Philadelphia (CHOP). Downstream analysis of the scRNA-seq samples was performed using Seurat (v. 4.3.0) in R (v. 4.2.2). Standard preprocessing was performed to remove cells with low counts or high percentage mitochondrial reads. Independent samples were merged or integrated and counts for all genes were $\log_2$ normalized and scaled. Principal components (PCs) were determined using the 2,000 most variable genes. Subsequently, the top 20–50 PCs were used for graph-based clustering and dimensionality reduction by t-distributed stochastic neighbor embedding (t-SNE) or uniform manifold approximation and projection (UMAP). Clusters were annotated using a combination of marker gene expression and the SingleR package, with the Immunological Genome Project (ImmGen) database as a reference. Differential expression testing was performed using the MAST test in the FindMarkers function unless otherwise stated. GO term enrichment of marker or differentially expressed genes was performed using the clusterProfiler R package. GSEA of specific clusters was performed using the fgsea or escape R packages. Preprocessed, publicly available human scRNA-seq datasets from Jerby-Arnon et al. (2018), (2021) were downloaded from the Single Cell Portal (https://singlecell.broadinstitute.org/single_cell) and analyzed in R as described above. Detailed scripts and parameters used for each step of the analysis will be published and available on GitHub (https://github.com/ianfolkert).

Bulk RNA-seq analysis

Total RNA was isolated using GenElute Mammalian Total RNA Miniprep Kit with DNAse I digestion (Sigma-Aldrich). Library preparation and high-throughput sequencing using Illumina sequencers to generate paired-end results was performed by Novogene. Quantification of raw counts of gene transcripts was performed using an alignment-free tool, Kallisto (https://pachterlab.github.io/kallisto/about) using standard settings. The raw count matrix was subsequently imported into Rstudio (R version 4.2.2) and used as input file for analysis with limma/voom. Kallisto was used to normalize and quantitate gene expression in transcripts-per-million through quasi-alignment. Differentially expressed genes were used as input for GO term enrichment using the clusterProfiler R package, and GSEA was performed on the ordered expression data using the clusterProfiler R package and the hallmark gene sets from MSigDB (https://www.gsea-msigdb.org/gsea/index.jsp). Detailed scripts and parameters used for each step of the analysis will be published and available on GitHub (https://github.com/ianfolkert).

Generation of gene-gene correlation plots for Ednrb and iTAM markers

Correlations between Ednrb expression and expression of selected stiTAM and pviTAM markers were generated and

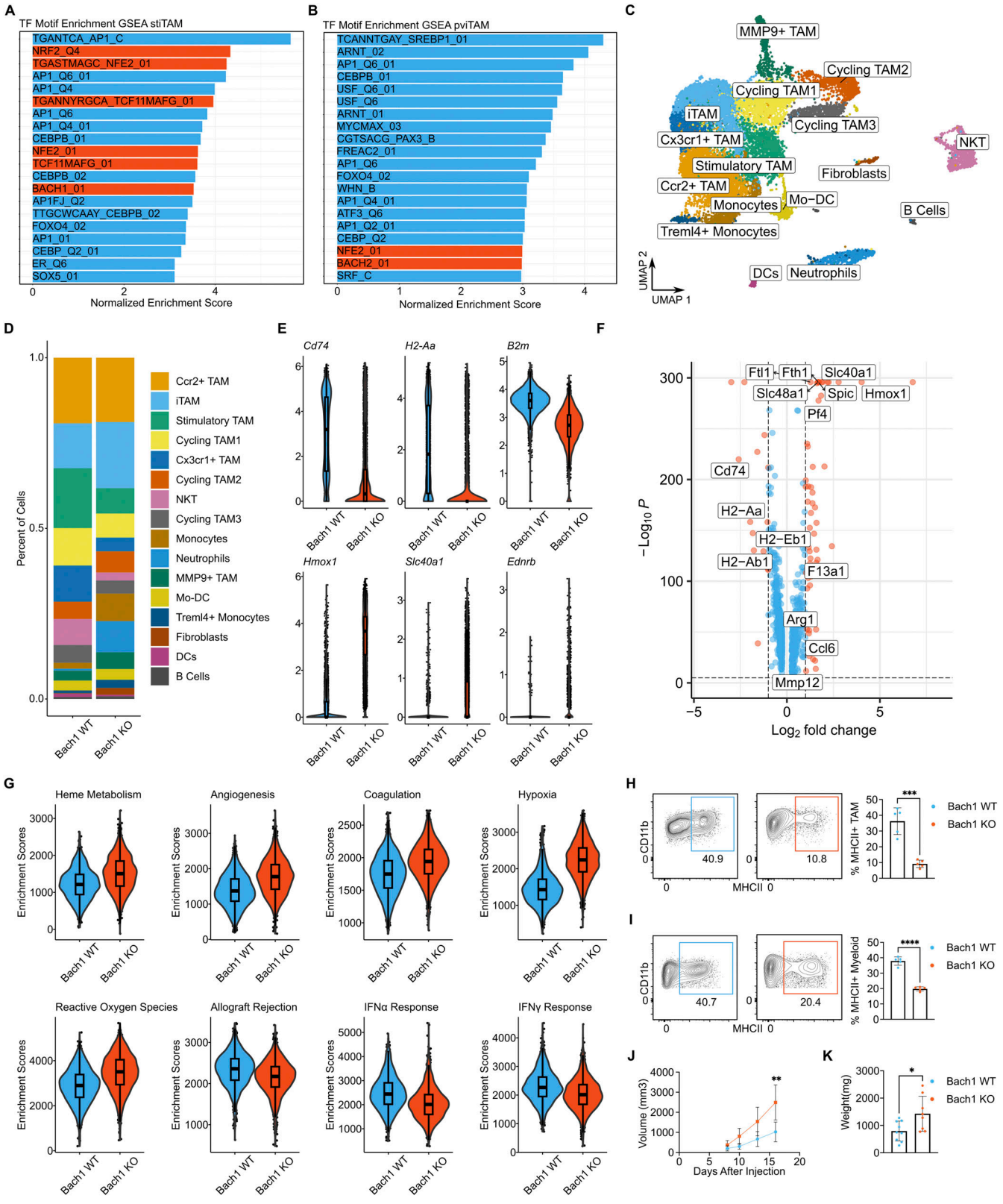

Figure 9. **Bach1 represses the iTAM phenotype. (A and B)** GSEA for transcription factor binding motif enrichment in stiTAM (A) and pviTAM (B) clusters in the iron fractionated TAM scRNA-seq dataset (described in Fig. 2 D) using the TFT_legacy subset of the TFT collection in MSigDB. Motifs related to Bach, Maf, and Nrf2 transcription factor binding are highlighted in red. **(C)** Annotated UMAP from integrated scRNA-seq dataset of CD45$^+$ column-enriched leukocytes from FS tumors generated in WT and Bach1 KO mice (Bach1 KO scRNA-seq dataset) (n = 1 mouse per genotype). Clusters are annotated using a combination of canonical marker genes and the SingleR package with the ImmGen database as a reference. **(D)** Percent contribution of each cluster by genotype in the Bach1 KO scRNA-seq dataset. **(E)** Expression of selected genes involved in antigen presentation (*Cd74*, *H2-Aa*, *B2m*), iron metabolism (*Hmox1*, *Slc40a1*), and *Ednrb* by

genotype in the Bach1 KO scRNA-seq dataset. **(F)** Volcano plot of differentially expressed genes between WT and Bach1 KO macrophages within the iTAM cluster of the Bach1 KO scRNA-seq dataset. Differentially expressed genes ($log_2FC > 1$ and P-adj < 0.05) are highlighted in red, with select genes involved in antigen presentation (*Cd74*, *H2-Aa*, *H2-Ab1*, *H2-Eb1*), iron metabolism (*Hmox1*, *Fth1*, *Ftl1*, *Slc40a1*, *Slc48a1*), known Bach1 target genes (*Spic*), and additional iTAM marker genes (*Pf4*, *F13a1*, *Arg1*, *Ccl6*, *Mmp12*) labeled. Differential expression testing was performed using MAST. **(G)** Violin plots showing GSEA enrichment scores for Bach1 WT and Bach1 KO iTAMs for indicated Hallmark pathways (headers). **(H)** FCM plots (left) and frequencies (right) of MHCII$^+$ TAMs (CD45$^+$CD11b$^+$F4/80^{high}) from littermate control (Bach1 WT) and Bach1 KO mice transplanted with FS tumors (n = 5 mice per group). Pregated on live singlets, CD45$^+$, Ly6G$^-$, CD11b$^+$, and F4/80^{high}. Representative of ≥2 independent experiments. **(I)** FCM plots (left) and frequencies (right) of MHCII$^+$ myeloid cells (CD45$^+$CD11b$^+$F4/80^{low}) from littermate control (Bach1 WT) and Bach1 KO mice transplanted with FS tumors (n = 5 mice per group). Pregated on live singlets, CD45$^+$, Ly6G$^-$, CD11b$^+$, and F4/80^{low}. Representative of ≥2 independent experiments. **(J)** FS flank tumor volumes from Bach1 WT and Bach1 KO mice (n = 4 mice per group). Representative of ≥3 independent experiments. **(K)** Tumor weight of FS flank tumors in Bach1 WT and Bach1 KO mice (n = 8 mice per group). *P < 0.05, **P < 0.01, ***P < 0.001, ****P < 0.0001. Statistical significance in H, I, and K was determined using the Mann-Whitney U test. Statistical significance in J was determined using repeated-measures ANOVA. Bar graphs are plotted as mean with SEM. All FCM plot events were pregated on live singlets unless otherwise specified and numbers represent percentage of cells within the highlighted gates.

downloaded directly using the cBioPortal (http://www.cbioportal.org/) for cancer genomics. All samples were compared to diploid samples when possible. Expression in RSEM log2 counts for soft tissue sarcoma (SARC)/lung adenocarcinoma (LUAD), microarray counts for invasive breast carcinoma (BRCA), and log_2 RPKM for colon adenocarcinoma (COAD). The r^2 value and P value for the Pearson and Spearman correlations are shown within each plot.

Generation of correlation plots for T cell dysfunction scores and iTAM markers

Heatmaps depicting Z-scores of T-cell dysfunction scores associated with each selected iTAM marker gene in both the Core and Immunotherapy datasets from the Tumor Immune Dysfunction and Exclusion (TIDE) database were generated directly through the TIDE online portal (https://tide.dfci.harvard.edu/).

Generation of tumor immune subtype plots

Raw data was downloaded from https://isb-cgc.shinyapps.io/shiny-iatlas/ as .csv files and plots were generated using ggplot2 in R studio (R version 4.2.2).

Implantation of tumor cells, tumor growth measurements

Cultured tumor cells were detached using 0.05% trypsin (GIBCO), washed once with DMEM media and once with 1× PBS, and counted in preparation for implantation. Tumor cells were propagated in vitro for two passages prior to implantation and injected cells were >90% viable. 1 × 10^6 tumor cells were implanted subcutaneously into shaved flanks of recipient mice. Tumor dimensions were measured using a caliper starting at day 7 or 8 and every 2–3 days thereafter; volume was calculated by using formula $(ab^2)/2$, where a is the longest measurement and b is the shortest.

Iron fractionation

Tumors were harvested, chopped, and single-cell suspensions were generated by digestion with collagenase B and DNAse I for 45 min at 37°C. Samples were filtered through a 70-µM cell strainer and RBC lysis was performed using ACK lysing buffer. Samples were resuspended in Magnetic-activated cell sorting (MACS) buffer (Miltenyi Biotec) and passed through a 70-µM cell strainer and onto an LS magnetic column (Miltenyi Biotec). After loading, cells were washed 3× with 3 ml of MACS buffer to collect the iron$^-$ fraction before removing the magnet from the column and eluting the iron$^+$ fraction with 5 ml of MACS buffer using a plunger. Both the iron$^-$ and iron$^+$ fractions were then enriched for macrophages using anti-F4/80 microbeads and column enrichment per protocol (Miltenyi Biotec).

Iron quantification

Single-cell suspensions were generated from the tumor or spleen through enzymatic digestion. The cell suspension was spun down (450 × *g* for 5 min) and resuspended in 400 µl of iron assay buffer. Cells were next sonicated (1 min/sample) and spun down at 1,300 × *g* for 5 min. The supernatant was collected and stored in −80°C freezer. Iron assay was performed on the stored supernatant using the Iron Assay Kit (catalog no: 83366; Abcam) and following the manufacturer's protocol.

FCM of murine samples

Tumors were harvested and cut into small pieces, and single-cell suspensions were generated by digestion with collagenase B and DNAse I for 45 min at 37°C and filtration through a 70-µM cell strainer. RBC lysis was performed using ACK lysing buffer. Samples were incubated for 5 min at room temperature with anti-mouse CD16/32 Fc Block and subsequently stained for 20 min at 4°C with primary fluorophore-conjugated antibodies for identification of cell populations by FACS. FCM was performed on a LSR II or a BD LSRFortessa Flow Cytometer (BD Biosciences) and analyzed using FlowJo software (Treestar).

Cell sorting

Cells were sorted on a MoFlo Astrios or FACS Jazz at the CHOP Flow Cytometry Core Laboratory. For measurement of gene expression in sorted cells, RNA was isolated from sorted cell pellets and RT-qPCR was performed as described elsewhere. For scRNA-seq experiments, sorted cells were resuspended in PBS + 1% FBS and submitted to the CHOP CAG for library preparation and sequencing as described above.

BMDM culture

BMDMs were generated by harvesting bone marrow from WT C57BL/6 mice. The long bones of the leg were cut and flushed with PBS to remove the marrow. RBCs lysis was performed using ACK lysing buffer. Cells were plated at a concentration of 1–2 × 10^6 cells per well in 6-well plates and cultured in M-CSF (20 ng/ml) for 5–7 days prior to treatment with indicated drugs or compounds.

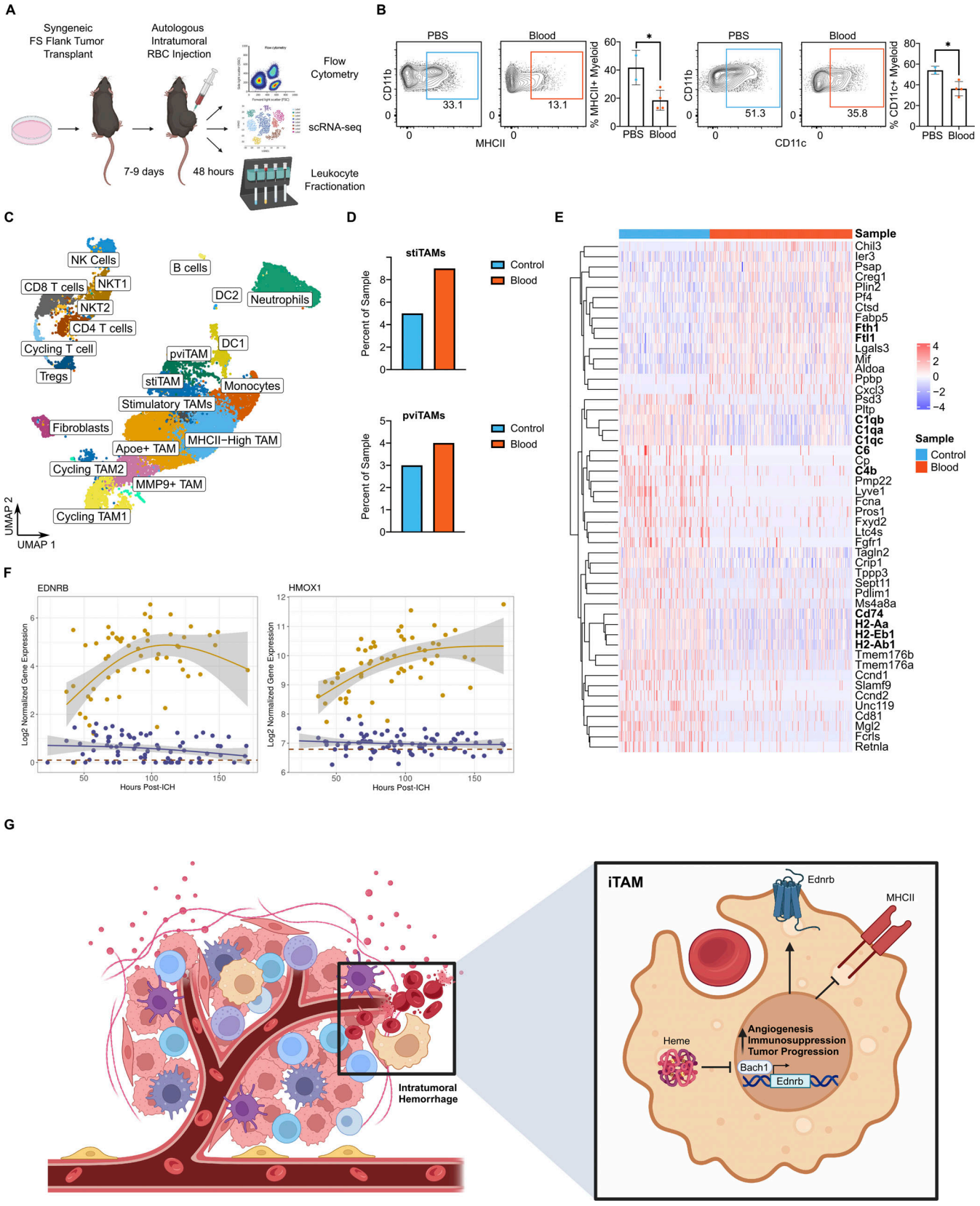

Figure 10. **Hemorrhage-derived heme regulates iTAM development. (A)** Schematic of the intratumoral autologous blood injection model and downstream analysis. **(B)** FCM plots showing expression of pro-inflammatory markers (MHCII and CD11c) in myeloid cells (CD11b^{high}) from PBS (control) and autologous blood injected FS tumors 48 h after injection (n = 4 mice per group). Cells pregated on live singlets, CD45$^+$ cells. Representative of ≥3 independent experiments. **(C)** CD45$^+$ leukocytes were FAC-sorted 48 h after PBS (control) or autologous blood injection of FS flank tumors (n = 2 mice per group) and profiled by scRNA-

seq. Shown are UMAP plots of the merged control and blood-injected samples after the two datasets were combined and annotated using a combination of canonical marker genes and reference-based annotation using SingleR, with the ImmGen database as a reference (merged hemorrhage scRNA-seq dataset). Cells from the replicates of each experimental group were combined before sequencing, yielding one sequencing dataset per group. **(D)** Percent contribution of stiTAMs and pviTAMs in the PBS (control) and autologous blood injected samples in the merged hemorrhage scRNA-seq dataset. **(E)** Heatmap of the top 50 significantly differentially expressed genes between PBS (control) and autologous blood injected cells in the pviTAM cluster of the merged hemorrhage scRNA-seq dataset. Genes involved in iron metabolism, antigen presentation, or the generation of immune or inflammatory responses are bolded. **(F)** Log_2 normalized expression over time of *EDNRB* and *HMOX1* in human peripheral blood monocytes (blue) and monocytes/macrophages from intracerebral hemorrhage (ICH) patients (gold) in a previously published dataset (Askenase et al., 2021). **(G)** Model for iTAM induction and function in the TME. *P < 0.05. Statistical significance was determined using the Mann-Whitney U test. Bar graphs are plotted as mean with SEM. All FCM plot events were pregated on live singlets unless otherwise specified and numbers represent percentage of cells within the highlighted gates.

Mouse and human monocyte differentiation assays

Mouse monocytes were isolated from bone marrow using the Mouse BM Monocyte Isolation Kit (Miltenyi Biotec) per protocol. Both viability and purity of the monocyte isolation protocol were confirmed to be >90% by FCM. Isolated monocytes were cultured in M-CSF (20 ng/ml) for 5 days prior to treatment. Normal donor human monocytes (obtained from the Human Immunology Core at the University of Pennsylvania) were cultured in M-CSF (50 ng/ml) for 5 days prior to treatment. Murine and human cytokines were purchased from PeproTech.

T cell proliferation assays

Murine macrophages were isolated from FS tumors using anti-F4/80 microbeads (Miltenyi Mouse Anti-F4/80 Microbeads UltraPure cat# 130-110-443) followed by sorting F4/80^{high} FOLRB^{high} macrophages using Bio-Rad S3e Cell Sorter. Isolated tumor macrophages were cultured in 20 ng/ml M-CSF for 48 h before culturing with T cells. Total T cells were isolated from C57BL/6 mouse spleens using Pan T cell isolation kit (Miltenyi Mouse Pan T Cell Isolation Kit II cat# 130-095-130). T cells were stained with CellTrace Violet Cell Proliferation Kit (CTV, cat#C34557; Thermo Fisher Scientific) and then activated with Dynabeads Mouse T-Activator CD3/CD28 for T-Cell Expansion and Activation (cat#11456D; Thermo Fisher Scientific). CTV-stained T cells were then cultured with sorted macrophages at a 1:2 ratio in round-bottom 96-well plates for 72 h. CTV dilution was measured using FCM.

Angiogenesis assays

Glioblastoma-derived primary endothelial cells were cultured in endothelial cell media (cat#1001; ScienCell) to >70% confluency. Cells were then co-cultured for 4–12 h at 37°C with 5% oxygen with sorted tumor macrophages or BMDMs at a 1:2 ratio in 200 µl of endothelial cell media in chamber slides that were precoated with 200 µl of Matrigel (Corning Matrigel Basement Membrane Matrix, LDEV (lactose dehydrogenase elevating virus) -free, 10 ml, cat# 354234).

Depletion of CD3$^+$ T cells in vivo

200 µg of clone 17A2 (CD3$^+$ T cell depletion) was administered i.p. three days prior to tumor transplant and repeated every 3 days until the end of the experiment. Anti-CD3 antibodies were purchased from BioXCell. CD3$^+$ T Cell depletion was confirmed within tumors by FCM.

RNA isolation and RT-qPCR analysis for gene expression

Total RNA was isolated using the GenElute Mammalian Total RNA Miniprep Kit (Sigma-Aldrich). cDNA was generated using the High-Capacity RNA to cDNA Kit (Life Technologies). RT-qPCR was performed using ViiA7 Real-Time PCR machine and TaqMan probes used for gene-specific amplification (purchased from Thermo Fisher Scientific) are: Arg1 (Mm00475988_m1), Ciita (Mm00482914_m1), Hmox1 (Mm00516005_m1), Slc40a1 (Mm01254822_m1), Ednrb (Mm00432989_m1), Spic (Mm00488428_m1), Bach1 (Mm01344527_m1), Hprt (Mm03024075_m1), Ednrb (Hs00240747_m1), Slc40a1 (Hs00205888_m1), Spic (Hs00745166_m1), and Hprt (Cat #4333768).

Immunohistochemistry

Tissue samples were fixed in 4% paraformaldehyde (Santa Cruz) at 4°C overnight before washing 2× with PBS and preserving in 70% EtOH. Samples were then submitted to the Molecular Pathology and Imaging Core at the University of Pennsylvania for paraffin embedding. After rehydration, blocking of endogenous peroxidases, and antigen retrieval using Vector Laboratories H-3300 Citrate-Based Antigen Unmasking Solution, pH 6 (Vector Laboratories), tissue was blocked with 5% bovine serum albumin (BSA) and 0.1% Tween-20 in TBS for 1 h at room temperature followed by overnight incubation with primary antibody diluted in TBS with 1% BSA and 0.1% Tween-20 in a humidified chamber. The following day, sections were washed three times with TBS with 1% BSA and 0.1% Tween-20. Sections were then incubated with biotinylated secondary antibodies (Jackson ImmunoResearch) before developing with the ABC HRP and DAB kits per protocol (Vector Laboratories). Primary antibodies used were as follows: rabbit anti-Ednrb (NLS54; Novus) and goat anti-CD31 (AF3628).

Immunofluorescence

Tissue samples were fixed in 4% paraformaldehyde for 12 h. Tissue samples were then incubated in 15 and 30% sucrose until sunken in solution. Subsequently, samples were embedded in OCT and cryopreserved in −80°C. After sectioning, samples were stained using the following protocol: Tissues were washed twice with 1X PBS for 5 min at room temperature. A blocking solution was added containing 10% BSA in PBS-Tween 0.05% for 30 min. Samples were washed once in 1X PBS. Primary antibodies were diluted in a blocking solution and incubated overnight at 4°C in a humidified chamber. Tissue samples were then washed three times with 1X PBS followed by incubation with secondary antibodies diluted in blocking solution for 1 h at room temperature before imaging. Primary antibodies used were as follows: rabbit anti-Ednrb (NLS54; Novus), goat anti-

CD31 (AF3628), rat anti-CD68 (ab53444), and rabbit anti-Hmox1(ab52947).

Image analyses for cell quantification

Immunohistochemistry sections were scanned using a high-resolution Aperio digital pathology scanner. Image analysis was processed in QuPath software version 0.2.345. Cell detection and quantification of CD31-positive cells were assessed using QuPath's built-in positive cell detection tool. Immunofluorescence images were scanned with Aperio digital pathology scanner and images were processed using ImageJ software version 2.14.0/1.54f. Angiogenesis assay chamber slides were imaged using EVOS5000 microscope. Images were analyzed using Angiogenesis Analyzer plugin in ImageJ software version 2.14.0/1.54f.

Xenium in situ workflow

Gene panel design

A custom probe panel based on Xenium human skin panel and in-house scRNA-seq data from human melanoma biopsies targeting 350 genes including melanoma, immune, fibroblast, neural, neural crest, mesenchymal, stem cell phenotypes, and negative controls for cell type identification was designed.

Xenium sample preparation

To start Xenium workflow 5 µm Formalin Fixed Paraffin Embedded (FFPE) tissue sections were sectioned onto Xenium slides, followed by deparaffinization and permeabilization. The mRNAs were targeted by the custom probe panel and control probes. Overnight probe hybridization was performed at 50°C with a probe concentration of 10 nM. Stringent posthybridization washes were carried out to remove unhybridized probes. Probe ligation was done at 37°C for 2 h, when a rolling circle amplification primer was also annealed. Circularized probes were then amplified for 2 h at 37°C enzymatically to generate copies of the gene-specific barcode for each RNA binding event. Washing and chemical quenching of background fluorescence was carried out followed by nuclei staining with DAPI. Sections on the cassette were loaded onto the Xenium Analyzer instrument.

Xenium Analyzer instrument

On the Xenium Analyzer, image acquisition was performed in cycles by automatically cycling in reagents and labeled probes for detecting RNA. These were incubated on the sections, imaged, and removed by the instrument. After binding fluorescent oligos to the amplified barcode sequence, 15 rounds of fluorescent probe hybridization, imaging, and probe removal were performed. The Z-stack images spanning 0.75-µm step size across the entire tissue thickness were taken.

Image processing and analysis

The Xenium Analyzer captured a Z-stack of images every cycle and in every channel, which was processed and stitched on the DAPI image, taking all of the stacks from different Fields of View (FOVs) and colors to create a single seamless image representative of one region of interest. This was used to build a spatial map of the transcripts across the tissue section. The pipeline was detected every punctum, which was measured in units of observed photons, in every cycle, every image, and every colors to observe all potential mRNA. A Gaussian distribution was fitted to the observed emitted light to localize puncta and those from different cycles occupying the same space were registered to one another. Fluorescently labeled oligonucleotides were bound to amplified barcodes and the fluorescent intensity in each of the four Xenium color channels was measured in each cycle. This was done for 15 Xenium cycles and was used to generate an optical signature unique for each gene. Each decoded transcript was assigned a Phred-scaled Quality Value called Q score. All Xenium spatial gene plots shown use transcripts passing Q ≥ 20. For cell segmentation, DAPI images were acquired, and each nucleus was expanded outward until either 15-µm max distance was reached or the boundary of another cell was reached. The on-instrument pipeline produced output files including the feature-cell matrix, the transcripts, the cell boundaries CSV file, and the differentially enriched gene list for each cluster. Further downstream analysis was performed off-instrument and visualized using Xenium Explorer.

Post-Xenium histology

H&E staining-post-Xenium sections were used for regular H&E staining, and the whole section was imaged at 20× magnification using Keyence microscope and stitched to generate a composite brightfield image at high resolution.

Cell–cell interaction analysis using CytoTalk

We used CytoTalk to infer cell–cell interactions between macrophages/iTAMs and the other cell types in a mouse synovial sarcoma scRNA-seq dataset. Normalized gene-by-cell expression matrix and cell type annotation were used as the input. For ligand/receptor gene expression in the target cell type, we set a minimum expression threshold of 10%. The interaction strength was predicted based on the cross-talk score. The interaction specificity was determined by the $-\log_{10}$(Pval_potential + 1e−10). Pval_potential was computed following a Gamma distribution model. L-R interactions with Pval_potential below 0.05 were considered significant.

Statistics

Sample sizes were based on previous publications and our experience with similar experiments. The numbers per experiment and repeats are listed in the figure legends. Statistical significance was calculated between the two groups by using the Student's unpaired *t*-test for normally distributed data and the Mann–Whitney U test for non-parametric data. One-way ANOVA with Tukey's HSD (Honestly Significant Difference) post-test was used to calculate statistical significance between multiple groups. Repeated-measures ANOVA was used to determine statistically significant differences in tumor volume. The significance for survival was calculated by Kaplan–Meier with

Table 1. **Reagents**

Reagent or Resource	Source	Clone	Identifier (RRID/ catalog number)	
Antibodies				
CD45	BD Biosciences	30-F11	AB_2651134	
CD11b	eBioscience	M1/70	AB_2896082	
Ly6C	Biolegend	HK1.4	AB_2562352	
MHCII	Biolegend	M5/ 114.15.2	AB_2561397	
F4/80	Biolegend	BM8	AB_2562305	
CD36	BD Biosciences	CRF D-2712	AB_2739064	
Ly6G	Biolegend	1A8	AB_10640452	
Lyve1	eBioscience	ALY7	AB_10597449	
CD163	Biolegend	S15049I	AB_2890710	
CD11c	Biolegend	N418	AB_830649	
Ednrb	Novus Biologicals	671917	AB_3096090	
Folrb	Biolegend	10/FR2	AB_2721343	
Hmox1 IF	Abcam	EP1391Y	ab52947	
CD68 IF	Abcam	FA-11	ab53444	
EDNRB IF	Novus Biologicals	Polyclonal	NLS54	
CD31 IF	R&D Systems	Polyclonal	AF3628	
CD31	Biolegend	390	AB_312900	
CD3	Biolegend	17A2	AB_1732057	
CD4	Biolegend	GK1.5	AB_10900241	
PD1	Biolegend	RMP1-30	AB_313421	
FOXP3	eBiosciences	FJK-16 s	AB_914349	
Granzyme B	Biolegend	GB11	AB_2566333	
InVivoMAb anti-mouse PD-1 (CD279)	Bio X Cell	RMP1-14	AB_10949053	
InVivoMab anti-mouse CD3	Bio X Cell	17A2	AB_1107630	
CD16/32 Fc Block	BD Biosciences	2.4G2	AB_394656	
Chemicals, peptides and recombinant proteins				**Sequence**
CTV	Invitrogen		C34557	
Zombie NIR	Biolegend		423105	
Macitentan	MedChemExpress		HY-14184	
Endothelin 1, human, HiLyte Fluor 488-labeled	AnaSpec		AS-64817-025	HiLyte Fluor 488-CSCSSLMDKECVYFCHLDIIW (Disulfide Bridge: 1–15 and 3–11)
CD45 MicroBeads, mouse	Miltenyi Biotec	30F11.1	130-052-301	
Anti-F4/80 MicroBeads UltraPure, mouse	Miltenyi Biotec		130-110-443	
Pan T Cell Isolation Kit II, mouse	Miltenyi Biotec		130-095-130	
Monocyte Isolation Kit (BM), mouse	Miltenyi Biotec		130-100-629	
Recombinant Murine M-CSF	PeproTech		315-02	
Recombinant Human M-CSF	PeproTech		300-25	
TAT-CRE Recombinase	Sigma-Aldrich		SCR508	
Hemin	Sigma-Aldrich		51280	
Trypsin-EDTA (0.25%), phenol red	Gibco		25200056	

Table 1. **Reagents (*Continued*)**

Reagent or Resource	Source	Clone	Identifier (RRID/ catalog number)
Dynabeads Mouse T-Activator CD3/CD28 for T-Cell expansion and Activation	Gibco		11452D
LS Columns, MACS Cell separation	Miltenyi Biotec		130-042-401
DNase I	Sigma-Aldrich		D4527-200KU
Collagenase B	Sigma-Aldrich		11088831001
RBC Lysis Buffer, 10X	Santa Cruz Biotechnology		sc-296258
Vector Laboratories H-3300 Citrate-Based Antigen Unmasking Solution, pH 6	Vector Laboratories		H-3300-250
Critical commercial assays			
Iron Assay Kit (Colorimetric)	Abcam		ab83366
GenElute Mammalian Total RNA Miniprep Kit with DNAse I digestion	Sigma-Aldrich		RTN70-1KT
High-Capacity RNA-to-cDNA Kit	Thermo Fisher Scientific		4387406
Experimental models: Cell lines and animal models			
FS B6PRG			
UPS			
Synovial			
qPCR probes (ThermoFisher Taqman gene expression assays)	**Assay ID**		
Mouse			
Ednrb	Mm00432989_m1		
Arg1	Mm00475988 m1		
Ciita	Mm00482914_m1		
Hmox1	Mm00516005_m1		
Slc40a1	Mm01254822_m1		
Bach1	Mm01344527_m1		
Spic	Mm00488428_m1		
Hprt	Mm03024075_m1		
Human			
EDNRB	Hs00240747_m1		
SPIC	Hs00745162_s1		
HPRT	Hs99999909_m1		
SLC40A1	Hs00205888_m1		

log-rank analysis. Analyses were performed using GraphPad Prism 9. Error bars represent SEM and $P < 0.05$ was considered statistically significant (*$P < 0.05$, **$P < 0.01$, ***$P < 0.001$).

Study approval

All animal experiments were approved by the Institutional Animal Care and Use Committee at the University of Pennsylvania (Protocol no. 805728). Deidentified human specimens were under an approved Institutional Review Board protocol at The University of Texas MD Anderson Cancer center.

Reagents

Reagents are listed in Table 1.

Online supplemental material

Fig. S1 shows TAM subsets enriched for heme metabolism. Fig. S2 shows Characterizing iTAM subsets. Fig. S3 shows Ednrb expression in iTAM subsets. Fig. S4 shows Ednrb function in iTAMs. Fig. S5 shows Regulation of Ednrb expression by the heme-Bach1 axis. Table S1 shows Xenium probe detais. Table S2 shows Xenium transcript abundance.

Data availability

The datasets generated in this study have been submitted to the Gene Expression Omnibus (GEO) and the accession numbers are GSE269437, GSE268581, GSE269203, GSE269145, GSE268866, GSE268865.

Acknowledgments

We thank Drs. Brian Keith and Ronald DeMatteo for their valuable scientific input. We also thank the FCM cores at UPenn and CHOP, CAG Core at CHOP, and Human Immunology Core (HIC) at UPenn. We are grateful to the MelCore at The University of Texas MD Anderson Cancer Center for providing us with data from human melanoma samples.

This work was supported by the Cancer Research Institute Llyod J STAR award (M. Haldar), Burroughs Wellcome Fund CAMS award (M. Haldar), Concern Foundation (M. Haldar), AACR-Bayer Innovation and Discovery Grant (M. Haldar), Slay Sarcoma Foundation research grant (M. Haldar), Measey Foundation Surgeon Scientist Training Grant (I.W. Folkert), T32 training grant (T32 DK007780, National Institute of Diabetes and Digestive and Kidney Diseases at National Institutes of Health) to W.A. Molina Arocho, and American College of Surgeons Resident Research Scholarship (I.W. Folkert).

Author contributions: I.W. Folkert: Conceptualization, Data curation, Formal analysis, Investigation, Methodology, Project administration, Software, Validation, Visualization, Writing—original draft, Writing—review & editing, W.A. Molina Arocho: Conceptualization, Data curation, Formal analysis, Investigation, Methodology, Validation, Visualization, Writing—original draft, Writing—review & editing, T.K.J. To: Investigation, S. Devalaraja: Data curation, I.S. Molina: Resources, J. Shoush: Formal analysis, Investigation, Methodology, H. Mohei: Investigation, Resources, Software, Validation, Visualization, L. Zhai: Investigation, M.N. Akhtar: Data curation, Formal analysis, Investigation, V. Kochat: Data curation, Investigation, Writing—original draft, E. Arslan: Formal analysis, Software, A.J. Lazar: Data curation, Investigation, Writing—review & editing, K. Wani: Data curation, Methodology, W. Padron: Investigation, Z. Zhang: Formal analysis, Methodology, V.S. Chaluvadi: Investigation, Writing—review & editing, R.J. Norgard: Conceptualization, Resources, Writing—review & editing, Y. Liu: Resources, A.M. Fuller: Investigation, M.T. Dang: Writing—review & editing, R.E. Roses: Conceptualization, Data curation, Writing—original draft, G.C. Karakousis: Conceptualization, Resources, Supervision, Writing—review & editing, J.T. Miura: Methodology, D.L. Fraker: Resources, Writing—review & editing, T.S.K. Eisinger-Mathason: Conceptualization, M.C. Simon: Conceptualization, Supervision, Writing—review & editing, K. Weber: Writing—review & editing, K. Tan: Funding acquisition, Methodology, Software, Supervision, Y. Fan: Methodology, Writing—review & editing, K. Rai: Supervision, M. Haldar: Conceptualization, Data curation, Formal analysis, Funding acquisition, Methodology, Project administration, Resources, Supervision, Validation, Visualization, Writing—original draft, Writing—review & editing.

Disclosures: K. Rai reported personal fees from Daiichi Sankyo, other from Jivanu Therapeutics, and other from Koshika Therapeutics outside the submitted work. No other disclosures were reported.

Submitted: 8 March 2023
Revised: 4 April 2024
Accepted: 7 August 2024

References

Alam, M.Z., S. Devalaraja, and M. Haldar. 2017. The heme connection: Linking erythrocytes and macrophage biology. *Front. Immunol.* 8:33. https://doi.org/10.3389/fimmu.2017.00033

Arlauckas, S.P., C.S. Garris, R.H. Kohler, M. Kitaoka, M.F. Cuccarese, K.S. Yang, M.A. Miller, J.C. Carlson, G.J. Freeman, R.M. Anthony, et al. 2017. In vivo imaging reveals a tumor-associated macrophage-mediated resistance pathway in anti-PD-1 therapy. *Sci. Transl. Med.* 9:eaal3604. https://doi.org/10.1126/scitranslmed.aal3604

Askenase, M.H., B.A. Goods, H.E. Beatty, A.F. Steinschneider, S.E. Velazquez, A. Osherov, M.J. Landreneau, S.L. Carroll, T.B. Tran, V.S. Avram, et al. 2021. Longitudinal transcriptomics define the stages of myeloid activation in the living human brain after intracerebral hemorrhage. *Sci. Immunol.* 6:eabd6279. https://doi.org/10.1126/sciimmunol.abd6279

Benci, J.L., B. Xu, Y. Qiu, T.J. Wu, H. Dada, C. Twyman-Saint Victor, L. Cucolo, D.S.M. Lee, K.E. Pauken, A.C. Huang, et al. 2016. Tumor interferon signaling regulates a multigenic resistance program to immune checkpoint blockade. *Cell.* 167:1540–1554.e12. https://doi.org/10.1016/j.cell.2016.11.022

Chakarov, S., H.Y. Lim, L. Tan, S.Y. Lim, P. See, J. Lum, X.-M. Zhang, S. Foo, S. Nakamizo, K. Duan, et al. 2019. Two distinct interstitial macrophage populations coexist across tissues in specific subtissular niches. *Science.* 363:eaau0964. https://doi.org/10.1126/science.aau0964

Chen, D.S., and I. Mellman. 2013. Oncology meets immunology: The cancer-immunity cycle. *Immunity*. 39:1–10. https://doi.org/10.1016/j.immuni.2013.07.012

Chen, G., B. Ning, and T. Shi. 2019. Single-cell RNA-seq Technologies and related computational data analysis. *Front. Genet.* 10:317. https://doi.org/10.3389/fgene.2019.00317

Dagamajalu, S., D.A.B. Rex, L. Gopalakrishnan, G. Karthikkeyan, S. Gurtoo, P.K. Modi, V. Mohanty, M. Mujeeburahiman, S. Soman, R. Raju, et al. 2021. A network map of endothelin mediated signaling pathway. *J. Cell Commun. Signal.* 15:277–282. https://doi.org/10.1007/s12079-020-00581-4

DeNardo, D.G., and B. Ruffell. 2019. Macrophages as regulators of tumour immunity and immunotherapy. *Nat. Rev. Immunol.* 19:369–382. https://doi.org/10.1038/s41577-019-0127-6

Devalaraja, S., and M. Haldar. 2020. Intratumoral monocyte transfer to examine monocyte differentiation in the tumor microenvironment. *STAR Protoc.* 1:100188. https://doi.org/10.1016/j.xpro.2020.100188

Devalaraja, S., T.K.J. To, I.W. Folkert, R. Natesan, M.Z. Alam, M. Li, Y. Tada, K. Budagyan, M.T. Dang, L. Zhai, et al. 2020. Tumor-derived retinoic acid regulates intratumoral monocyte differentiation to promote immune suppression. *Cell.* 180:1098–1114.e16. https://doi.org/10.1016/j.cell.2020.02.042

Gubin, M.M., E. Esaulova, J.P. Ward, O.N. Malkova, D. Runci, P. Wong, T. Noguchi, C.D. Arthur, W. Meng, E. Alspach, et al. 2018. High-dimensional analysis delineates myeloid and lymphoid compartment remodeling during successful immune-checkpoint cancer therapy. *Cell.* 175:1014–1030.e19. https://doi.org/10.1016/j.cell.2018.09.030

Haldar, M., J.D. Hancock, C.M. Coffin, S.L. Lessnick, and M.R. Capecchi. 2007. A conditional mouse model of synovial sarcoma: Insights into a myogenic origin. *Cancer Cell.* 11:375–388. https://doi.org/10.1016/j.ccr.2007.01.016

Haldar, M., M. Kohyama, A.Y.-L. So, W. Kc, X. Wu, C.G. Briseño, A.T. Satpathy, N.M. Kretzer, H. Arase, N.S. Rajasekaran, et al. 2014. Heme-mediated SPI-C induction promotes monocyte differentiation into iron-recycling macrophages. *Cell.* 156:1223–1234. https://doi.org/10.1016/j.cell.2014.01.069

Haldar, M., and K.M. Murphy. 2014. Origin, development, and homeostasis of tissue-resident macrophages. *Immunol. Rev.* 262:25–35. https://doi.org/10.1111/imr.12215

Hashizume, H., P. Baluk, S. Morikawa, J.W. McLean, G. Thurston, S. Roberge, R.K. Jain, and D.M. McDonald. 2000. Openings between defective endothelial cells explain tumor vessel leakiness. *Am. J. Pathol.* 156:1363–1380. https://doi.org/10.1016/S0002-9440(10)65006-7

Hu, Y., T. Peng, L. Gao, and K. Tan. 2021. CytoTalk: De novo construction of signal transduction networks using single-cell transcriptomic data. *Sci. Adv.* 7:eabf1356. https://doi.org/10.1126/sciadv.abf1356

Igarashi, K., and M. Watanabe-Matsui. 2014. Wearing red for signaling: The heme-bach axis in heme metabolism, oxidative stress response and iron immunology. *Tohoku J. Exp. Med.* 232:229–253. https://doi.org/10.1620/tjem.232.229

Jerby-Arnon, L., C. Neftel, M.E. Shore, H.R. Weisman, N.D. Mathewson, M.J. McBride, B. Haas, B. Izar, A. Volorio, G. Boulay, et al. 2021. Opposing immune and genetic mechanisms shape oncogenic programs in synovial sarcoma. *Nat. Med.* 27:289–300. https://doi.org/10.1038/s41591-020-01212-6

Jerby-Arnon, L., P. Shah, M.S. Cuoco, C. Rodman, M.-J. Su, J.C. Melms, R. Leeson, A. Kanodia, S. Mei, J.-R. Lin, et al. 2018. A cancer cell program promotes T cell exclusion and resistance to checkpoint blockade. *Cell.* 175:984–997.e24. https://doi.org/10.1016/j.cell.2018.09.006

Kalbasi, A., and A. Ribas. 2020. Tumour-intrinsic resistance to immune checkpoint blockade. *Nat. Rev. Immunol.* 20:25–39. https://doi.org/10.1038/s41577-019-0218-4

Kirsch, D.G., D.M. Dinulescu, J.B. Miller, J. Grimm, P.M. Santiago, N.P. Young, G.P. Nielsen, B.J. Quade, C.J. Chaber, C.P. Schultz, et al. 2007. A spatially and temporally restricted mouse model of soft tissue sarcoma. *Nat. Med.* 13:992–997. https://doi.org/10.1038/nm1602

Lapenna, A., M. De Palma, and C.E. Lewis. 2018. Perivascular macrophages in health and disease. *Nat. Rev. Immunol.* 18:689–702. https://doi.org/10.1038/s41577-018-0056-9

Lee, J., A.E. Yesilkanal, J.P. Wynne, C. Frankenberger, J. Liu, J. Yan, M. Elbaz, D.C. Rabe, F.D. Rustandy, P. Tiwari, et al. 2019. Effective breast cancer combination therapy targeting BACH1 and mitochondrial metabolism. *Nature.* 568:254–258. https://doi.org/10.1038/s41586-019-1005-x

Lignitto, L., S.E. LeBoeuf, H. Homer, S. Jiang, M. Askenazi, T.R. Karakousi, H.I. Pass, A.J. Bhutkar, A. Tsirigos, B. Ueberheide, et al. 2019. Nrf2 activation promotes lung cancer metastasis by inhibiting the degradation of Bach1. *Cell.* 178:316–329.e18. https://doi.org/10.1016/j.cell.2019.06.003

Liu, Z., Y. Gu, S. Chakarov, C. Bleriot, I. Kwok, X. Chen, A. Shin, W. Huang, R.J. Dress, C.-A. Dutertre, et al. 2019. Fate mapping via Ms4a3-expression history traces monocyte-derived cells. *Cell.* 178:1509–1525.e19. https://doi.org/10.1016/j.cell.2019.08.009

Motz, G.T., and G. Coukos. 2013. Deciphering and reversing tumor immune suppression. *Immunity.* 39:61–73. https://doi.org/10.1016/j.immuni.2013.07.005

Murray, P.J. 2017. Macrophage polarization. *Annu. Rev. Physiol.* 79:541–566. https://doi.org/10.1146/annurev-physiol-022516-034339

Nelson, J.B., S.P. Hedican, D.J. George, A.H. Reddi, S. Piantadosi, M.A. Eisenberger, and J.W. Simons. 1995. Identification of endothelin-1 in the pathophysiology of metastatic adenocarcinoma of the prostate. *Nat. Med.* 1:944–949. https://doi.org/10.1038/nm0995-944

Noy, R., and J.W. Pollard. 2014. Tumor-associated macrophages: From mechanisms to therapy. *Immunity.* 41:49–61. https://doi.org/10.1016/j.immuni.2014.06.010

Pfefferlé, M., G. Ingoglia, C.A. Schaer, A. Yalamanoglu, R. Buzzi, I.L. Dubach, G. Tan, E.Y. López-Cano, N. Schulthess, K. Hansen, et al. 2020. Hemolysis transforms liver macrophages into antiinflammatory erythrophagocytes. *J. Clin. Invest.* 130:5576–5590. https://doi.org/10.1172/JCI137282

Pitt, J.M., M. Vétizou, R. Daillère, M.P. Roberti, T. Yamazaki, B. Routy, P. Lepage, I.G. Boneca, M. Chamaillard, G. Kroemer, and L. Zitvogel. 2016. Resistance mechanisms to immune-checkpoint blockade in cancer: Tumor-intrinsic and -extrinsic factors. *Immunity.* 44:1255–1269. https://doi.org/10.1016/j.immuni.2016.06.001

Qian, B.-Z., and J.W. Pollard. 2010. Macrophage diversity enhances tumor progression and metastasis. *Cell.* 141:39–51. https://doi.org/10.1016/j.cell.2010.03.014

Rattner, A., H. Yu, J. Williams, P.M. Smallwood, and J. Nathans. 2013. Endothelin-2 signaling in the neural retina promotes the endothelial tip cell state and inhibits angiogenesis. *Proc. Natl. Acad. Sci. USA.* 110:E3830–E3839. https://doi.org/10.1073/pnas.1315509110

Riaz, N., J.J. Havel, V. Makarov, A. Desrichard, W.J. Urba, J.S. Sims, F.S. Hodi, S. Martín-Algarra, R. Mandal, W.H. Sharfman, et al. 2017. Tumor and microenvironment evolution during immunotherapy with nivolumab. *Cell.* 171:934–949.e16. https://doi.org/10.1016/j.cell.2017.09.028

Said, N., S. Smith, M. Sanchez-Carbayo, and D. Theodorescu. 2011. Tumor endothelin-1 enhances metastatic colonization of the lung in mouse xenograft models of bladder cancer. *J. Clin. Invest.* 121:132–147. https://doi.org/10.1172/JCI42912

Soares, M.P., and I. Hamza. 2016. Macrophages and iron metabolism. *Immunity.* 44:492–504. https://doi.org/10.1016/j.immuni.2016.02.016

Sun, J., M. Brand, Y. Zenke, S. Tashiro, M. Groudine, and K. Igarashi. 2004. Heme regulates the dynamic exchange of Bach1 and NF-E2-related factors in the Maf transcription factor network. *Proc. Natl. Acad. Sci. USA.* 101:1461–1466. https://doi.org/10.1073/pnas.0308083100

Svensson, V., K.N. Natarajan, L.-H. Ly, R.J. Miragaia, C. Labalette, I.C. Macaulay, A. Cvejic, and S.A. Teichmann. 2017. Power analysis of single-cell RNA-sequencing experiments. *Nat. Methods.* 14:381–387. https://doi.org/10.1038/nmeth.4220

Thorsson, V., D.L. Gibbs, S.D. Brown, D. Wolf, D.S. Bortone, T.-H. Ou Yang, E. Porta-Pardo, G.F. Gao, C.L. Plaisier, J.A. Eddy, et al. 2018. The immune landscape of cancer. *Immunity.* 48:812–830.e14. https://doi.org/10.1016/j.immuni.2018.03.023

Vinchi, F., M. Costa da Silva, G. Ingoglia, S. Petrillo, N. Brinkman, A. Zuercher, A. Cerwenka, E. Tolosano, and M.U. Muckenthaler. 2016. Hemopexin therapy reverts heme-induced proinflammatory phenotypic switching of macrophages in a mouse model of sickle cell disease. *Blood.* 127:473–486. https://doi.org/10.1182/blood-2015-08-663245

Yin, J.J., K.S. Mohammad, S.M. Käkönen, S. Harris, J.R. Wu-Wong, J.L. Wessale, R.J. Padley, I.R. Garrett, J.M. Chirgwin, and T.A. Guise. 2003. A causal role for endothelin-1 in the pathogenesis of osteoblastic bone metastases. *Proc. Natl. Acad. Sci. USA.* 100:10954–10959. https://doi.org/10.1073/pnas.1830978100

Zhou, J., Z. Tang, S. Gao, C. Li, Y. Feng, and X. Zhou. 2020. Tumor-associated macrophages: Recent insights and therapies. *Front. Oncol.* 10:188. https://doi.org/10.3389/fonc.2020.00188

JEM

Supplemental material

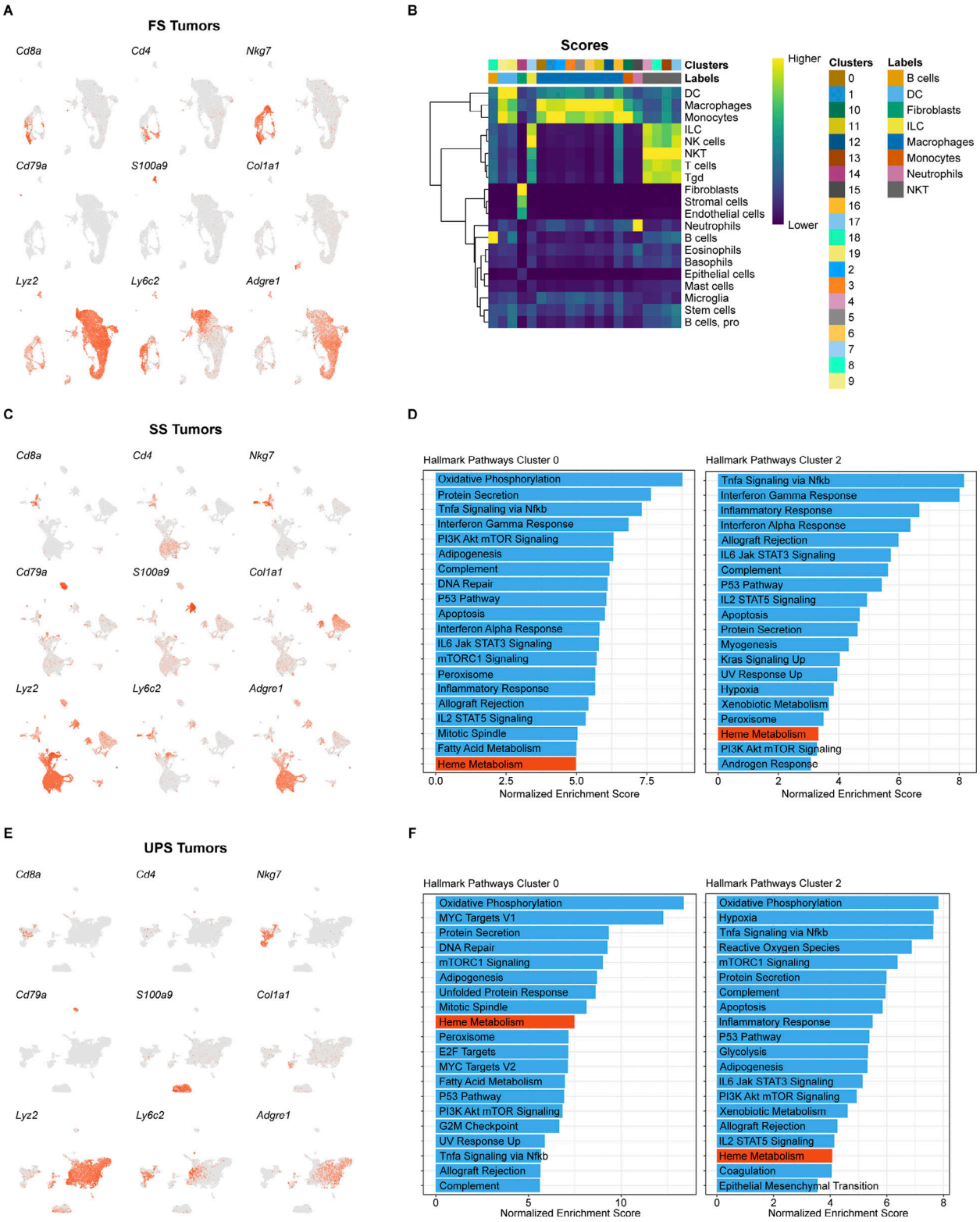

Figure S1. **TAM subsets enriched for heme metabolism. (A)** UMAP expression plots of marker genes specific to major leukocyte and stromal cell types in the murine FS scRNA-seq dataset. **(B)** Heatmap of SingleR scores for each cluster in the murine FS scRNA-seq dataset, using the ImmGen database as a reference for cell-type-specific gene expression signature. **(C)** UMAP expression plots of marker genes specific to major leukocyte and stromal cell types in the murine SS scRNA-seq dataset. **(D)** GSEA of clusters 0 and 2 (iTAMs, corresponding to encircled cells in Fig. 1 G) relative to all other clusters in the murine SS scRNA-seq dataset, with normalized enrichment scores of the top 20 Hallmark gene sets from the MSigDB shown. Gene sets related to heme metabolism are highlighted in red. **(E)** UMAP expression plots of marker genes specific to major leukocyte and stromal cell types in the murine UPS scRNA-seq dataset. **(F)** GSEA of clusters 0 and 2 (iTAMs, corresponding to encircled cells in Fig. 1 I) relative to all other clusters in the murine UPS scRNA-seq dataset, with normalized enrichment scores of the top 20 Hallmark gene sets from the MSigDB shown. Gene sets related to heme metabolism are highlighted in red.

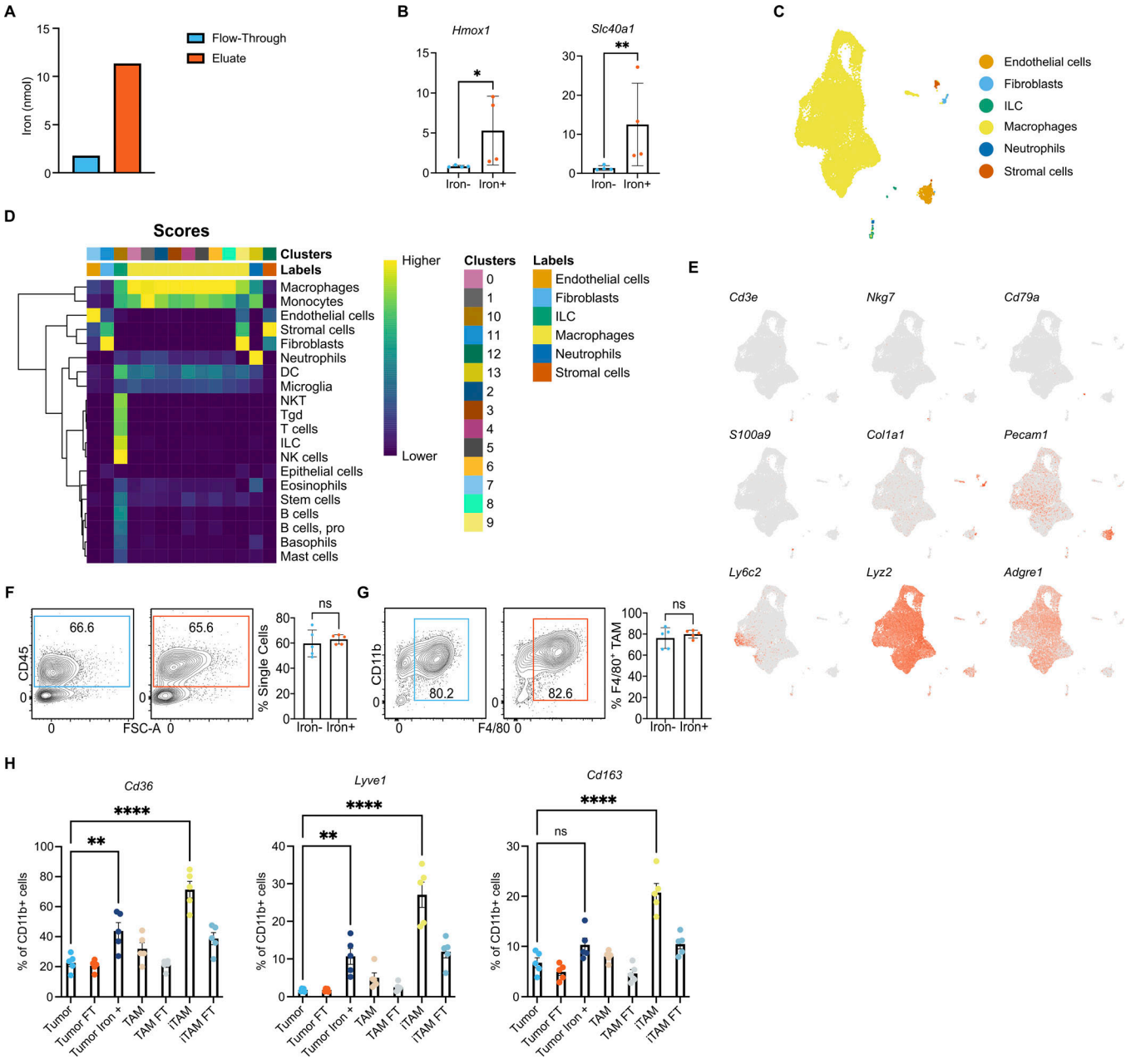

Figure S2. **Characterizing iTAM subsets. (A)** Iron quantification (Abcam) of iron-negative (flow-through) and iron-positive (eluate) cells isolated from mouse spleen. The workflow is similar to that depicted in Fig. 2 A, except that the second step of F4/80 enrichment was omitted for spleen samples. **(B)** Relative expression (RT-qPCR) of *Hmox1* and *Slc40a1* in iron fractionated TAMs isolated as described in Fig. 2 A (n = 4 independent tumors). **(C)** UMAP of iron-negative (flow-through, n = 2 mice) and iron-positive (eluate, n = 2 mice) TAMs from Fig. 2 D showing cell type annotation generated using the SingleR package with the ImmGen database as a reference for cell-type-specific gene expression signature. **(D)** Heatmap of SingleR scores for each cluster in the iron fractionated TAM scRNA-seq dataset, using the ImmGen database as a reference for cell-type-specific gene expression signature. **(E)** Selected marker gene expression for major leukocyte and stromal cell types in the iron fractionated TAM scRNA-seq dataset shown in Fig. 2 D. **(F)** FCM plots (left) and frequencies (right) of CD45$^+$ cells in iron-negative and iron-positive TAMs fractionated from FS tumors as described in Fig. 2 A. Pregated on live singlets. Representative of ≥3 independent experiments. **(G)** FCM plots (left) and frequencies (right) of CD45$^+$CD11b$^+$F4/80^{high} TAMs in iron-negative and iron-positive TAMs fractionated from FS tumors as described in Fig. 2 A. Pregated on live singlets. Representative of ≥3 independent experiments. **(H)** Single-cell suspensions were generated from murine syngeneic subcutaneous FS tumors by enzymatic digestion and taken through the magnetic column-based iTAM enrichment protocol (as shown in Fig. 2 A). Shown is the expression of key iTAM surface markers detected via FCM at each step of the enrichment. Tumor: unfractionated single-cell suspension from tumors. Tumor FT: flow-through after unfractionated tumor cells are run over the magnetic column for the first time. Tumor Iron+: iron-enriched fraction after unfractionated tumor cells are run over a magnetic column for the first time. TAM: Tumor FT sample incubated with ferromagnetic anti-F4/80 and run over magnetic columns to enrich for iron-negative TAM. TAM-FT: flow-through from the TAM step that contains F4/80-negative iron-negative cells. iTAM: Tumor iron+ fraction described above incubated with ferromagnetic anti-F4/80 and run over magnetic columns to enrich for iTAM. iTAM-FT: flow-through from the iTAM step that contains F4/80-negative iron-positive cells. *P < 0.05, **P < 0.01, ****P < 0.0001. Statistical significance in B, F, and G was determined using the Mann–Whitney U test. Significance for differences in H was determined using repeated-measures ANOVA. Bar graphs are plotted as mean with SEM. All FCM plot events were pregated on live singlets unless otherwise specified and numbers represent percentage of cells within the highlighted gates.

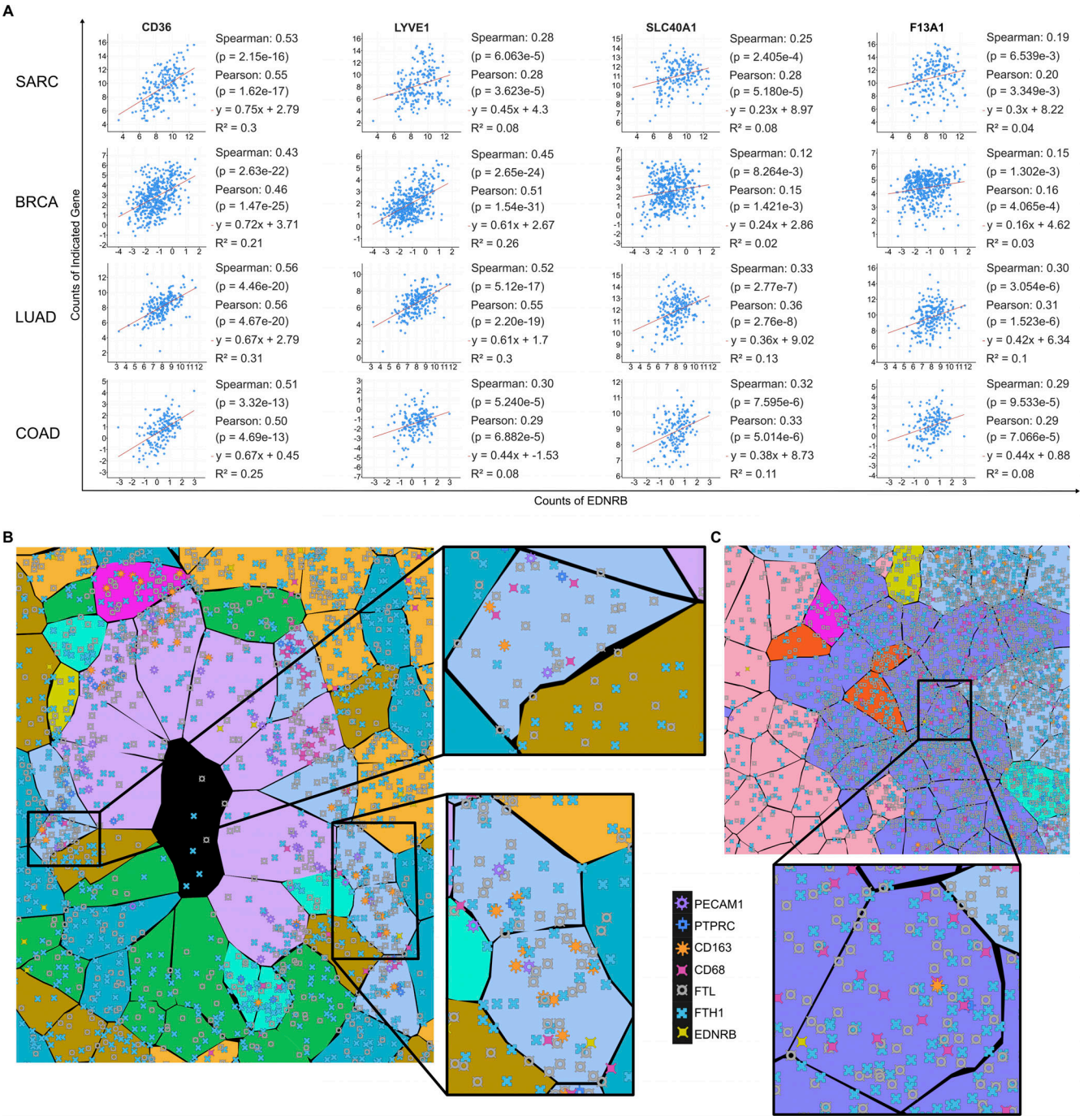

Figure S3. **Ednrb expression in iTAM subsets. (A)** Correlation between expression of *EDNRB* and selected iTAM-associated marker genes in the TCGA sarcoma (SARC), breast cancer (BRCA), lung adenocarcinoma (LUAD), and colon adenocarcinoma (COAD) datasets. Spearman and Pearson correlation coefficients are shown with associated P values. **(B)** Zoomed-in perivascular region from the Xenium spatial analyses of human melanoma described in Fig. 5 C. Color-coded cells reflect cell clusters identified by unbiased clustering analysis. Purple represents endothelial cells and sky blue pviTAMs (magnified inset). As shown in the figure, each gene/transcript is represented by a unique shape and its abundance by the frequency of that shape in a cell. **(C)** Zoomed-in stromal region from the Xenium spatial analyses of human melanoma described in Fig. 5 C. As described above, cell clusters and transcripts are coded by color and shape respectively. Purple cells here represent stiTAMs and are highlighted in the magnified inset.

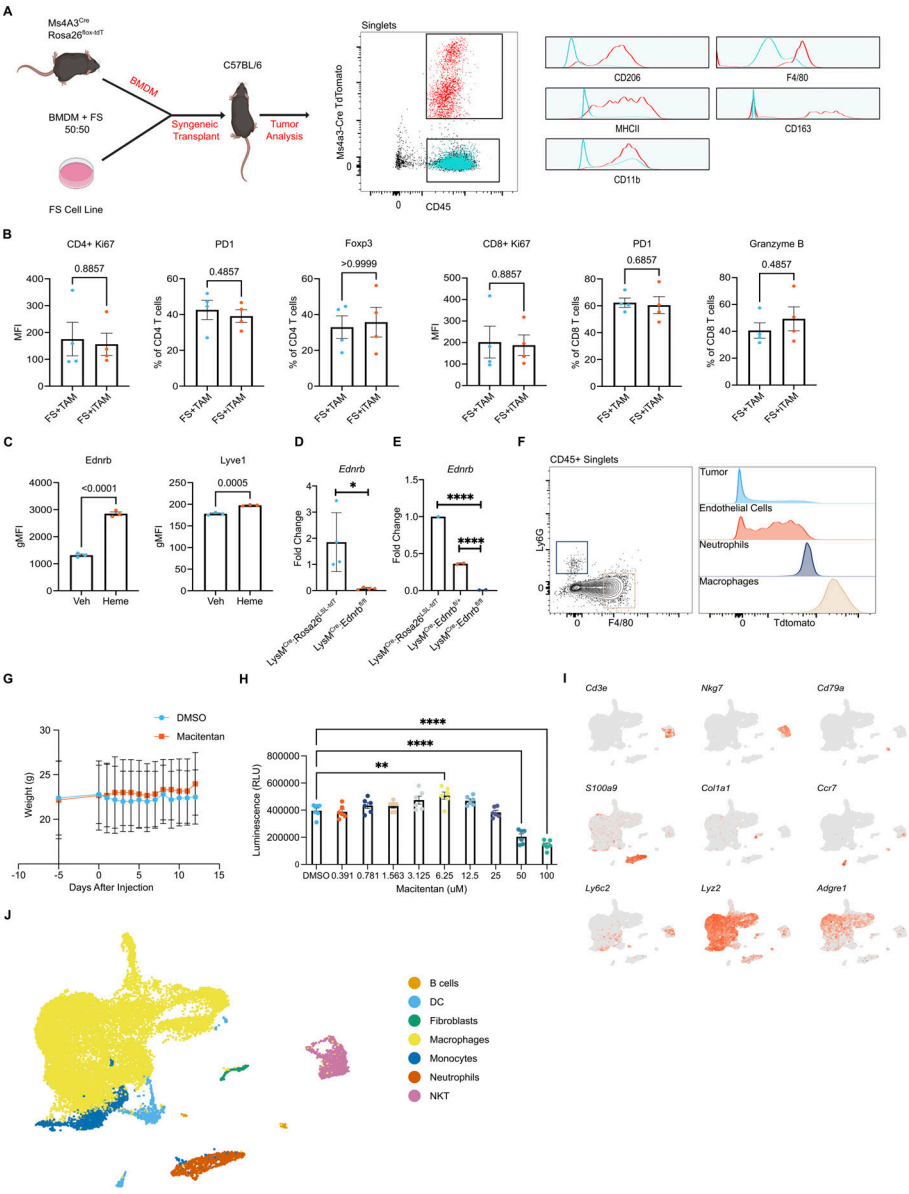

Figure S4. **Ednrb function in iTAMs. (A)** Bulk bone marrow cells from Ms4A3^{Cre}:Rosa26$^{Flox\text{-}tdT}$ mice were cultured in M-CSF to generate BMDMs. FS tumor cells were mixed with these BMDMs at a 50:50 ratio and subcutaneously transplanted into syngeneic C57BL/6J mice. FS tumors were harvested 14 days after transplantation and subjected to FCM to identify monocyte-derived macrophages (TdTomato-positive cells). Representative FCM is shown with the gating scheme for each histogram. The two-color histograms on the right show the distribution of Tdtomato+ (red) and Tdtomato− (blue) cells expressing macrophage markers CD206, F4/80, MHCII, CD163, and CD11b. **(B)** Co-transplantation of tumor cells with TAMs or iTAMs (as described in Fig. 6 G) was performed and the tumors were harvested on day 14. CD4 and CD8 T cell phenotyping was performed using FCM. The bar graphs show the various phenotypic parameters (y-axis) of indicated (header) cell types. *n* = 4 mice per group. Representative of ≥3 independent experiments. **(C)** FCM surface expression of key iTAM markers, Ednrb and Lyve1, by induced iTAMs (BMDMs exposed to heme). Three replicates per group. Representative of ≥3 independent experiments. **(D)** Relative expression (RT-qPCR) of *Ednrb* in FAC-sorted TAMs from subcutaneous FS tumors generated in control (Lysm^{Cre}:Rosa26$^{LSL\text{-}tdT}$) and Ednrb-KO (LysM^{Cre}:Ednrb$^{fl/fl}$) mice, confirming loss of *Ednrb* expression in Ednrb-KO TAMs. *n* = 4 mice per group. Representative of ≥3 independent experiments. **(E)** Relative expression (RT-qPCR) of *Ednrb* in FAC-sorted large peritoneal macrophages (CD45^{+}CD11b^{+}F4/80^{high}tdT^{+}) from either control (LysM^{Cre}:Rosa26$^{LSL\text{-}tdT}$), Ednrb-Het (LysM^{Cre}:Ednrb$^{+/flox}$:Rosa26$^{LSL\text{-}tdT}$), or Ednrb-KO (LysM^{Cre}:Ednrb$^{fl/fl}$:Rosa26$^{LSL\text{-}tdT}$) mice. Representative of ≥3 independent experiments. **(F)** The left panel shows the gating strategy for tumor-associated macrophages (TAMs) and neutrophils from FS tumors generated in Lysm^{Cre}:Rosa26$^{LSL\text{-}tdT}$ mice. Histograms show the expression of tdTomato (Lysm^{Cre}+ cells) in TAMs, neutrophils, endothelial cells, and tumor cells from these tumors. **(G)** Body weight was measured over time for WT mice injected with FS flank tumors and treated with either DMSO or the endothelin receptor antagonist Macitentan (see Fig. 8, E and F). *n* = 5 mice per group. Representative of ≥3 independent experiments. **(H)** CellTiter-Glo viability assay for FS cells treated with either DMSO or increasing concentrations of Macitentan in culture. Six replicates per group. Representative of ≥2 independent experiments. **(I)** UMAP expression plots of marker genes specific to major leukocyte and stromal cell types in the Bach1 KO scRNA-seq dataset. **(J)** UMAP of the murine Bach1 KO scRNA-seq dataset showing cell-type annotation using the SingleR package with the ImmGen database as a reference. *P < 0.05, **P < 0.01, ****P < 0.0001. Statistical significance in B–D was determined using the Mann–Whitney U test. Significance for differences in E and H was determined using repeated-measures ANOVA. Bar graphs are plotted as mean with SEM. All FCM plot events were pregated on live singlets unless otherwise specified and numbers represent percentage of cells within the highlighted gates.

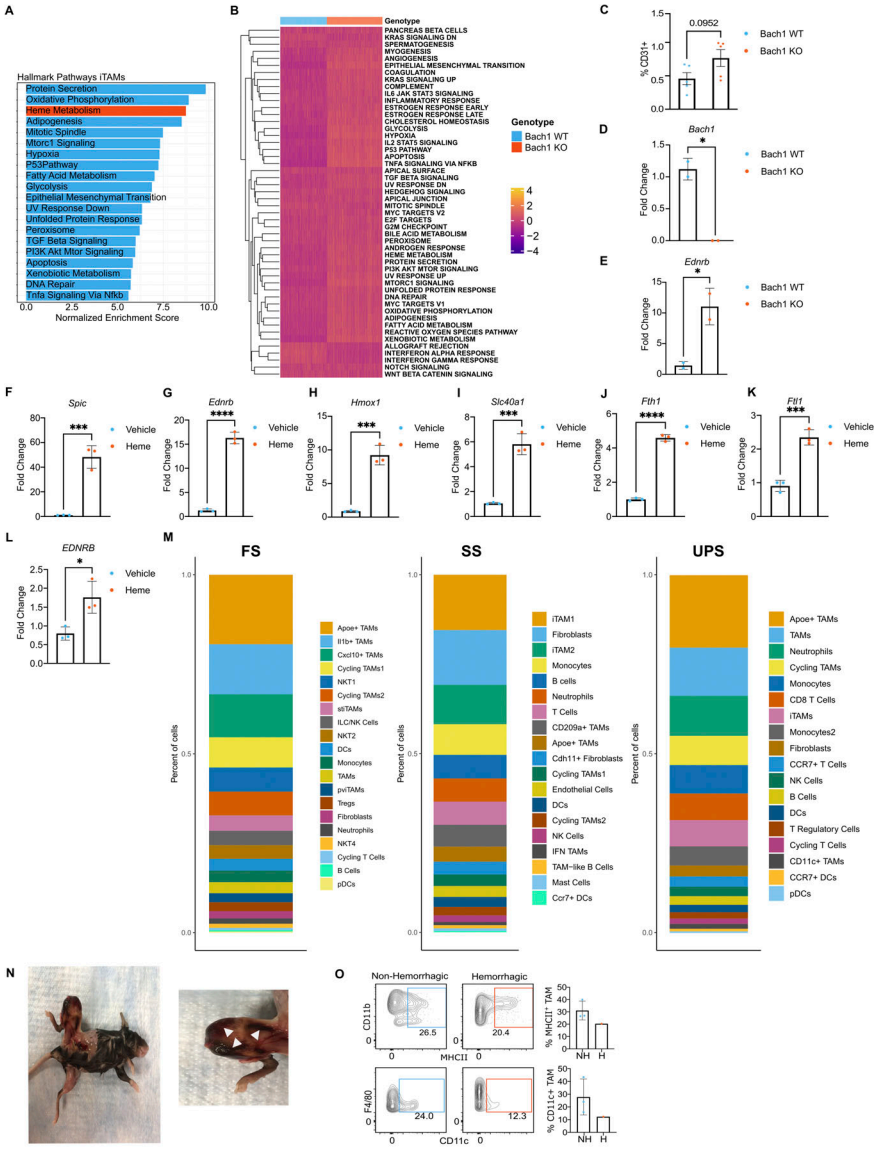

Figure S5. **Regulation of Ednrb expression by the heme-Bach1 axis. (A)** GSEA of the iTAM cluster in the murine Bach1 KO scRNA-seq dataset relative to all other clusters, with normalized enrichment scores of the top 20 Hallmark gene sets from the MSigDB shown, and the Heme metabolism gene set highlighted in red. **(B)** Heatmap of GSEA Hallmark pathway (MSigDB) enrichment comparing Bach1 WT and Bach1 KO cells within the iTAM cluster of the Bach1 KO scRNA-seq dataset. **(C)** FS flank tumors from Bach1 WT and Bach1 KO mice were harvested and the single-cell suspensions from the tumors were analyzed by FCM. Shown is the frequency of $CD45^{-}CD31^{+}$ endothelial cells as a percentage of all viable cells in the tumor (see also Fig. 9, J and K). *n* = 5 mice per group. Representative of ≥3 independent experiments. **(D)** Relative expression (RT-qPCR) of *Bach1* in mouse monocyte-derived macrophages (MDMs) from either WT littermate control (Bach1 WT) or Bach1 KO mice. MDMs were generated by isolating monocytes from bone marrow and culturing them with M-CSF. Representative of ≥3 independent experiments. **(E)** Relative expression (RT-qPCR) of *Ednrb* in mouse MDMs from either WT littermate control (Bach1 WT) or Bach1 KO mice. **(F)** Relative expression (RT-qPCR) of *Spic* in mouse BMDMs treated with vehicle control or Heme for 24 h. Representative of ≥3 independent experiments. **(G)** Relative expression (RT-qPCR) of *Ednrb* in mouse BMDMs treated with vehicle control or Heme for 24 h. Representative of ≥3 independent experiments. **(H)** Relative expression (RT-qPCR) of *Hmox1* in mouse BMDMs treated with vehicle control or Heme for 24 h. Representative of ≥3 independent experiments. **(I)** Relative expression (RT-qPCR) of *Slc40a1* in mouse BMDMs treated with vehicle control or Heme for 24 h. Representative of ≥3 independent experiments. **(J)** Relative expression (RT-qPCR) of *Fth1* in mouse BMDMs treated with vehicle control or Heme for 24 h. Representative of ≥3 independent experiments. **(K)** Relative expression (RT-qPCR) of *Ftl1* in mouse BMDMs treated with vehicle control or Heme for 24 h. Representative of ≥3 independent experiments. **(L)** Relative expression (RT-qPCR) of *EDNRB* in human MDMs treated with vehicle control or Heme for 24 h. Representative of ≥3 independent experiments. **(M)** Percent contribution of each cluster of cells identified by unbiased analyses of scRNA-seq data of $CD45^{+}$ cells from the different tumor types indicated above each bar graph. FS tumors were generated by a syngeneic transplant of FS tumor cells into $LysM^{Cre}$:$Rosa26^{LSL\text{-}tdT}$ (control/WT) recipient mice. SS and UPS are autochthonous tumors generated by TAT-Cre injection in genetically engineered mice. **(N)** Example of a spontaneously hemorrhagic murine SS tumor. Image on the right shows a magnified picture of an SS tumor. White arrowheads point towards the hemorrhagic areas. **(O)** FCM plots show frequency of $MHCII^{+}$ (top) and $CD11c^{+}$ (bottom) TAMs in non-hemorrhagic (left) and spontaneously hemorrhagic (right) SS tumors and littermate controls. (NH: Non-hemorrhagic, H: Hemorrhagic). *P < 0.05, ***P < 0.001, ****P < 0.0001. Statistical significance was determined using the Mann–Whitney U test. Bar graphs are plotted as mean with SEM. All FCM plot events were pregated on live singlets unless otherwise specified and numbers represent the percentage of cells within the highlighted gates.

Provided online are two tables. Table S1 shows Xenium probe detais. Table S2 shows Xenium transcript abundance.